Helium Diffusion Systematics Inferred from Continuous Ramped Heating Analysis of Transantarctic Mountains Apatites Showing Age Overdispersion

Hongcheng Guo[a,*], Peter K. Zeitler[a], Bruce D. Idleman[a], Annia K. Fayon[b], Paul G. Fitzgerald[c], Kalin T. McDannell[d]

[a] Department of Earth and Environmental Sciences, Lehigh University, Bethlehem, PA 18015
[b] Department of Earth Sciences, University of Minnesota, Minneapolis, MN 55455
[c] Department of Earth and Environmental Sciences, Syracuse University, Syracuse, NY 13244
[d] Department of Earth Sciences, Dartmouth College, Hanover, NH 03755
* Corresponding author: Hongcheng Guo (hog217@lehigh.edu)

Keywords: Apatite; (U-Th)/He; Thermochronology; Age Dispersion; Helium; Diffusion; Transantarctic Mountains

ABSTRACT

Application of apatite (U-Th)/He thermochronology has been hindered by incomplete understanding of diffusion systematics that leads to the single-grain age dispersion often displayed by samples, particularly those from older, slowly cooled settings. We applied the continuous ramped heating (CRH) method to an apatite suite from Cathedral Rocks in the Transantarctic Mountains (TAM) that have high age dispersion in order to explain processes that complicate ^{4}He diffusion in apatite. Examining 132 apatite grains from a total of six samples, we confirmed earlier apatite (U-Th)/He results showing that measured AHe ages have at least three-fold intra-sample dispersion with no obvious relationships between ages and effective uranium concentration (eU) or grain size. CRH results on these apatites yielded two groups. Those with younger ages, characterized by unimodal incremental ^{4}He gas-release curves, displayed simple volume diffusion behavior. In contrast, grains with older ages generally show complex gas release in the form of sharp spikes and/or extended gas-release at high temperatures (i.e., >= 800 °C). Simply-behaved apatites still show considerable age dispersion that exceeds what grain size, radiation damage, and analytical uncertainty can explain, but this dispersion appears to be related to variations in ^{4}He diffusion kinetics. The screened AHe ages from simply-behaved younger apatite grains together with kinetic information from these grains suggest that the sampled region experienced slow cooling prior to rapid cooling (rock exhumation) beginning *ca.* 35 Ma. This interpretation is consistent with other studies indicative of an increase in exhumation rates at this time, possibly related to the initiation of glaciation at the Eocene-Oligocene climate transition. An attempt to correct older apatite ages by simply removing extraneous gas-release components yielded some ages that are too young for the samples' geologic setting, suggesting that the factors that lead to complex laboratory release behavior can impact both the expected radiogenic component as well as those that are apparently extraneous. From our observations, we infer that many apatite grains contain imperfections of varying kinds that contribute significantly to kinetic variability beyond that associated with radiation damage and conclude that: (1) CRH analysis can serve as a routine screening tool for AHe dating and

offers opportunities to reveal first-order kinetic variations; (2) model-dependent age correction may be possible but would require some means of estimating the broad proportions of ^{4}He components incorporated into grains before and after closure to diffusion, and (3) interpretation of highly dispersed AHe ages requires assessment of individual-grain diffusion kinetics beyond that predicted by radiation-damage models.

1. Introduction

Following the proposal that apatite (U-Th)/He (AHe) ages could be used as a low-temperature thermochronometer (Zeitler et al., 1987), advances in pursuing the fundamental diffusion systematics and kinetics of helium release (Wolf et al., 1996; Farley et al., 1996; Farley, 2000; Shuster et al., 2006; Flowers et al., 2009) has led apatite (U-Th)/He thermochronology to become widely used in studies of tectonic and surface processes (e.g., Reiners et al., 2003; Reiners et al., 2005; Fitzgerald et al., 2006; Flowers and Farley, 2012; Toraman et al., 2014; Long et al., 2015). However, it has become widely recognized that interpretation of AHe data is often complicated by intra-sample age variations (commonly referred to as “excess age dispersion”) that are beyond typical analytical uncertainties (e.g., Fitzgerald et al., 2006; Flowers and Kelley, 2011; Peyton et al., 2012; Zeitler et al. 2017a; McDannell et al., 2018). Significant efforts have been made to explain such age dispersion and to unravel complexities in ^{4}He diffusion systematics. Some factors, for example, the presence of U-rich micro-inclusions (Farley, 2002), U and Th zonation (Meesters and Dunai, 2002; Fitzgerald et al., 2006), and ^{4}He implantation (Spiegel et al., 2009; Murray et al., 2014) will complicate He analysis or diffusion systematics in ways that make it difficult to obtain useful apparent ages (Farley, 2000). Other effects such as grain size (Reiners and Farley, 2001), broken grains, (Beucher et al., 2013; Brown et al., 2013), and the way that radiation damage systematically alters He diffusion kinetics (Shuster et al., 2006; Gautheron et al., 2009; Flowers et al., 2009; Willett

et al., 2017) can lead to age dispersion that can be exploited to reveal more information about thermal history. Slow cooling through or long-term residence within an apatite He partial retention zone will accentuate age dispersion, often to a considerable degree (e.g., Reiners and Farley, 2001; Fitzgerald et al., 2006).

Despite these contributions, there are still situations where we still cannot fully explain commonly observed AHe age dispersion. Applied studies of sample suites from different geologic settings have found that even using careful sample selection, grain size and radiation damage can only explain some of the observed dispersion (Zeitler et al., 2017a). To reduce the probability of overdispersed ages and to understand age dispersion should this occur, common practices include performing “re-extracts” to evaluate if all He has been out-gassed, collecting data only from single grains, performing large-n replicate analyses, and plotting He ages vs. size (radius) and effective uranium [eU] to evaluate excess dispersion. If excess dispersion occurs, complex data sets can be vexing and difficult to interpret and use in thermal history modeling, and if a large number of samples and single-grain analyses are undertaken in order to circumvent such issues, these approaches are time-consuming and costly.

As a result, the thermochronology community is actively working on the challenge that excess age dispersion presents (e.g., Zeitler et al., 2017b; McDannell et al., 2018). A possible factor in age dispersion that has attracted recent attention is the role that crystal imperfections of various types can play in changing diffusion behavior (Djimbi et al., 2015; Gerin et al., 2017; Zeitler et al., 2017b; Fayon and Hansen, 2018), adding to the impact that imperfections associated with radiation damage have on diffusion kinetics. This focus

is not a new concept, as Farley (2000) argued that *"Regardless of model, a critical question for apatite helium thermochronometry is whether the total abundance of defects affects the helium retentivity in the low temperature regime and, if so, how and when the defects are acquired."*

Here, we use a recently developed analytical approach, continuous ramped heating (hereafter, CRH, Idleman et al., 2018) which is described in **section 2.3**, to assess this long-standing problem of excess AHe age dispersion by closely examining samples from a well-characterized geological setting. In a broad survey of natural samples, McDannell et al. (2018) suggested that CRH should be able to identify variable ^{4}He outgassing behavior in the form of differing gas-release components. Our work aims to test this suggestion using a classic sample suite (Fitzgerald et al., 2006) from the Ferrar Glacier area of southern Victoria Land in the Transantarctic Mountains that yielded highly dispersed AHe ages (section 2.1). By better documenting how CRH can reveal relationships between AHe ages and ^{4}He outgassing behavior such that it can be deployed as a routine sample-characterization tool to extract interpretable data from complex sample sets, we seek to expand our understanding of the nature of He diffusion systematics in apatite.

2. Study Material and Analytical Methods

2.1. The Transantarctic Mountain apatite suite

Ideal apatite samples for our study should (1) have significant dispersed AHe ages, which is not uncommon, but also (2) be constrained by other thermochronological and geological information to allow assessment and interpretation of the dispersed ages. The

Transantarctic Mountains are a good locality to test our questions because their tectonic and thermochronological setting is relatively well established and their overall history of slow cooling since the Mesozoic will tend to amplify any dispersion in AHe ages which may be due to variations in ^{4}He diffusion systematics. We have selected a vertical profile collected from basement granitoids in the Ferrar Glacier area of southern Victoria Land in the Transantarctic Mountains – Cathedral Rocks – because of its thermal history, as well as the availability of both AHe and apatite fission track (hereafter, AFT) age constraints from previous studies (e.g., Fitzgerald 1992, 2002). Those studies suggest the locality also experienced relatively rapid cooling early in the Oligocene, possibly resulting from the onset of glacial incision or a change in tectonics.

The Transantarctic Mountains (TAM; **Fig. 1)** have long been regarded as an intriguing feature owing to their large size (>2500 km long), high elevations (>4 km), and the way they define the western flank of the West Antarctic rift system, in essence separating the significantly different geological terranes of East and West Antarctica (e.g., Dalziel, 1992; Fitzgerald, 2002; Goodge, 2020). The West Antarctic rift system underwent two phases of extension, early initiation in the middle Mesozoic (e.g., Elliot and Fleming, 2004), and then a later post-Eocene phase (e.g., Wilson et al., 1998; Florindo et al., 2001; Smellie, 2001). In southern Victoria Land basement rock is dominated by the arc-related Cambro-Ordovician magmatic suite of the Granite Harbour Intrusives (e.g., Allibone et al., 1993) intruded into polydeformed metasedimentary rocks (e.g., Goodge, 2020) during the Ross Orogeny. Devonian to Triassic flat-lying sedimentary rocks known as the Beacon Supergroup were then deposited unconformably on a basement erosion surface. Basin sedimentation was subsequently ended by extensive basaltic flood magmatism marking

the breakup of Gondwana, expressed in southern Victoria Land as the Ferrar Dolerite, presenting as thick (~300 m) sills within the basement and along the unconformity, as well as thinner sills distributed within Beacon sediments (e.g., Gunn and Warren, 1962). Subsequent to Ferrar magmatism, the TAM was formed largely by uplift along the West Antarctic rift flank (e.g., Fitzgerald, 1992). Due to this rift-flank uplift, the layer-cake stratigraphy of the TAM dips (1-2°) gently inland before disappearing under the East Antarctica Ice Sheet (e.g., Gunn and Warren 1962; Goodge, 2020).

There is a rich collection of thermochronological studies in southern Victoria Land, both onshore (Gleadow et al., 1984; Gleadow and Fitzgerald, 1987; Fitzgerald and Gleadow, 1988; Fitzgerald 1992, 2002; Olivetti et al., 2018) and offshore (Fitzgerald 2001; Olivetti et al., 2013) that generally document episodic exhumation with periods of enhanced cooling and exhumation (though slow relative to most active orogens) in the Cretaceous and Cenozoic. Fitzgerald et al. (2006) sought to explore the younger part of the exhumation history (less than ca. 50 Ma) by integrating AFT data with inverse thermal models, combined with, what at that time, was the relatively new approach of apatite (U-Th)/He dating. However, apatite (U-Th)/He ages from two vertical profiles collected on either side of the Ferrar Glacier displayed considerable single-grain age variation (**Fig. 1)**. Thus, the focus of that study shifted from constraining the younger exhumation history of the TAM towards documenting and exploring why over-dispersion occurs and how such data might be interpreted. Nevertheless, constraints on the cooling and exhumation history of this part of the TAM were obtained. With less AHe age dispersion within data from the north side vertical profile (Peak 1880) the interpretation was more complete: slow cooling (exhumation) from Late Cretaceous to early Eocene (~1°C/Myr), an increase in

cooling rate at ca. 43 Ma, then slowing again until another increase in the late Eocene (ca 37–35 Ma). On the south side of the glacier, AHe data from a vertical profile from the eastern-most of the peaks of the Cathedral Rocks had much greater age dispersion than the Peak 1880 profile, thus the interpretation relied mainly on AFT data/models and the AHe ages added very little to our understanding of the younger cooling history. Apatites from Cathedral Rocks are therefore the focus of our current study. At Cathedral Rocks, the interpretation of Fitzgerald et al. (2006) was that cooling/exhumation was relatively slow (~1°C/Myr) from Cretaceous to the early Cenozoic, with slightly faster cooling/exhumation beginning ca. 50 Ma (~2.8 °C/Myr).

For CRH screening and AHe dating, apatite grains were selected from six samples from the Ferrar Glacier profile at Cathedral Rocks, originally labeled R22641, R22642, R22643, R22644, R22645, and R22646 from high to low elevation (Fitzgerald et al., 2006). To simplify communication, in the following discussion we refer to these as R1, R2, R3, R4, R5, R6, respectively. All apatite grains were picked, examined, and photographed using a Nikon SMZ800 microscope under plain light at ~95× magnification for optical characterization to determine shape and size for calculation of alpha-ejection correction factors and to assess basic grain characteristics such as presence of inclusions, euhedral-vs-anhedral shape, and grain integrity (see **Research Data – Table A1**).

2.2 Sample Characterization

2.2.1 Chemistry

To document their overall composition as well as chemical variability, we analyzed a number of grains from two samples (R1 and R2) by electron microprobe. Complete results

are found in the online archive; Table 1 summarizes results by averaging data for all spots for all grains. Only Si, Ce, and F show some modest scatter, but Si and Ce are present at low concentrations. The grains are all fluorapatite in composition, with an average proportion for Fap:Cap:Hap (Piccoli and Candela, 2002) of 0.859 : 0.007 : 0.133 . Values of the fission-track annealing parameter *rmr0* (Ketcham et al., 2007) calculated from the elemental analyses range from 0.829 to 0.840, signifying near-endmember fluorapatite (**Appendix A – Fig. A.1**).

	R1	**N=48 spots, 30 grains**			**R2**	**N=51 spots, 30 grains**		
	Mean	**SD**	**CDL99**	**MSWD**	**Mean**	**SD**	**CDL99**	**MSWD**
Si	0.126	0.051	0.006	188	0.150	0.056	0.010	200
Y	0.121	0.053	0.030	7.2	0.151	0.057	0.030	8.4
La	*0.044*	*0.031*	0.031	4.3	*0.035*	*0.028*	*0.030*	3.6
Ce	0.195	0.060	0.029	15.4	0.204	0.071	0.030	22.1
Mg	*0.003*	0.003	0.006	1.0	*0.008*	*0.015*	*0.010*	1.7
Ca	39.63	0.159	0.010	3.7	39.47	0.222	0.010	9.3
Sr	*0.014*	*0.007*	0.013	1.1	*0.014*	*0.008*	*0.010*	1.6
Na	*0.010*	*0.007*	0.009	2.2	*0.012*	*0.009*	*0.010*	2.2
P	18.53	0.139	0.014	2.0	18.44	0.125	0.010	1.8
S	*0.001*	0.002	0.006	0.8	*0.001*	*0.003*	*0.010*	1.0
Cl	0.059	0.027	0.009	13.0	0.043	0.023	0.010	3.3
F	3.179	0.203	0.032	54.0	3.290	0.197	0.030	48.0
O	38.62	0.15			38.44	0.16		
TOTAL	100.53	0.36			100.25	0.42		

Table 1. Electron microprobe analyses of apatites from samples R1 and R2. Means, standard deviations, and detection limits are in weight percent. CDL99: Concentration with 99% confidence-level detection limit. MSWD (mean square of weighted deviates) serves as a measure of scattering of values relative to instrument uncertainties. Values in italics are near or below detection limit.

2.2.2 Survey of crystallographic defects

We examined polished sections of grains from samples R1 and R2 to assess the prevalence of defects in TAM apatites. Before polishing, grains were annealed at 500 ˚C for 60 minutes to remove any fission tracks and then etched using two different solutions, a typical 5M HNO_3 solution commonly used for fission-track etching, and also a 0.5 M HNO_3 solution to focus on smaller more delicate structures. Details about the size distribution of defects are part of an ongoing study, but for this paper a key observation is that TAM apatite grains are highly variable in etchable defect density, ranging from nearly imperfection-free to being riddled with imperfections of various types (**Fig. 2**).

2.3 Data collection and analysis

Individual grains were placed in closed niobium tubes, degassed of their ^{4}He via the CRH method at the Lehigh University noble-gas geochronology lab (see below and **Appendix B** for details), and measured for parent U-Th-Sm isotopes via dissolution and isotope dilution at the Arizona Radiogenic Dating Laboratory with detailed procedures reported by Reiners and Nicolescu (2006).

2.3.1 Continuous ramped heating

The CRH method characterizes the diffusive loss of ^{4}He by continuous heating following a progressively increasing temperature schedule, typically at a fixed rate. Evolved He is measured continuously as a function of time and temperature (Idleman et al., 2018). Our early experiments (Idleman et al., 2018; McDannell et al., 2018) used a resistance furnace for heating, which we have now replaced with a fiber-coupled diode laser system. The laser provides more precise time and temperature control, less temperature lag (i.e., better response time), and lower loads of potentially interfering active gases coevolved

214 with He. Here we briefly outline the most recent analytical procedure of our
215 implementation of CRH and include complete documentation of this CRH procedure in
216 **Appendix B**. We also provide our observations made on the behavior of standard
217 Durango apatite to document the behavior of simple ^{4}He diffusion systematics as
218 measured by our newest application of the CRH method.

219 **2.3.2 Sample handling**

220 After being selected and photographed, each apatite grain was placed in a closed niobium
221 (Nb) tube, which had been cleaned and then degassed for 3 hours in a vacuum furnace
222 at 600 °C. The loaded tube was placed in a hand-made Nb foil envelope ~4 mm in
223 diameter that had also been prewashed and degassed. We used these small envelopes
224 to present an even, flat surface to the laser beam in order to achieve better temperature
225 control and measurement. The packages were placed in quartz-glass holders located in
226 a mobile sample rack that allows us to load multiple samples and analyze them without
227 breaking vacuum.

228 **2.3.3 Data collection**

229 Each CRH run was performed under static vacuum conditions with the mass
230 spectrometer directly open to the sample cell. At the beginning of an analysis, the
231 extraction line was isolated from its pumping system and the ^{4}He beam was measured
232 and recorded for 3 – 4 minutes, allowing us to estimate cold-blank accumulation rates
233 before the initiation of heating. After heating began, temperatures were recorded by an
234 optical pyrometer capable of measurement over a range of ~180 to >1200°C. Peaks at
235 masses 1, 2, 3, 4, and 28 were measured and recorded continuously using a Balzer

Prisma Plus quadrupole mass spectrometer. Besides ^{4}He, the peaks corresponding to H, H_2, HD, and N_2 were monitored because we have found that in some runs high levels of these active gases can have a moderate impact on ^{4}He sensitivity by attenuating the mass 4 beam at temperatures greater than 850 to 900 °C. Two SAES GP50 getter pumps (operated at 20°C and 300°C) were used to reduce the partial pressures of these active gases during analysis so that their effects on ^{4}He were never more than a few percent at high temperatures when hydrogen and nitrogen attain their highest partial pressures (up to 100x those seen in the cold background signal).

All samples were heated to a temperature of at least 800°C. Samples that continued to outgas ^{4}He at 800°C were heated further until they showed no additional ^{4}He contribution for at least 1 minute, or until they reached 1100°C (whichever came first). After allowing 2-3 minutes for sample cool-down and additional purification of the evolved ^{4}He, a metered aliquot of ^{4}He of ~2.22×10^{-13} mol was introduced from a pipette system to allow determination of the total ^{4}He by the method of standard additions. In some cases, this post-run cleanup step was preceded by a small increase in the total-release ^{4}He signal (rarely exceeding 5%), reflecting gettering of the active gas species suppressing ^{4}He sensitivity. This small suppression does not have a significant impact on relative patterns of CRH release behavior but is clearly important to eliminate before measuring the final ^{4}He abundance for accurate age determination.

2.3.4 Data reduction

During our CRH runs for the Cathedral Rocks apatites, individual crystals were heated at a fixed rate of 30°C/minute, and temperature and ^{4}He measurements were recorded

every 10 seconds. To smooth noise in the measured sample temperatures, particularly at low temperatures, we performed a rolling 11-point linear regression of the measured temperatures and registered the times of ^{4}He measurement blocks within the regressed temperature record through interpolation. In practice, sample temperatures determined in this way agree with the targeted setpoint temperatures defined by the heating schedule to within 2-3°C. The ^{4}He beam values were then corrected for dynamic background and evolved blank, yielding final CRH results in the form of tables of time, temperature, and corrected ^{4}He beam values. From these results we calculated the first derivative of fractional loss (*f*) to construct incremental ^{4}He loss curves (*df/dT vs T,* hereafter *df* as shorthand) and to extract kinetic data (ln(D/a_2), (1/s), and *10000/T* (K)) for each sample. These data are available in the data repository as **Table A2** and **Table A3**.

2.3.5 Expected behavior: Durango apatite

We carried out CRH analyses of Durango apatite, an apatite standard widely used by the thermochronology community known for its reproducibility in AHe age (McDowell et al., 2005) and ^{4}He diffusion kinetics (Farley, 2000) with two goals: using its degassing behavior as a benchmark for expected CRH gas-release patterns and using its kinetics to test analytical reproducibility. We performed CRH screening on grains that were either internal fragments or abraded spherical balls that were made from air abrasion of fragments using an apparatus similar to that described by Krogh (1982).

The spherical-equivalent radii (Ketcham et al., 2011) of our grains ranged from 99 to 118 μm for the shards and from 90 to 167 μm for the balls. Grains were chosen to provide variation in size and a fairly large ^{4}He signal to be measured. In general, *df* curves for

both the shards and balls (**Fig. 3A**) exhibit the simple and consistent unimodal peaks predicted by volume diffusion theory (see modeled ^{4}He outgassing behavior via volume diffusion under CRH in Idleman et al. (2018) and McDannell et al. (2018)). We intentionally include results from balls with varying radius to show the precision of our CRH temperature control. With the same heating schedule of 30°C/min, the larger grains show a slightly higher-temperature peak-gas release (McDannell et al., 2018) compared to medium-sized balls (**Fig. 3A**), and the peak-gas release occurred at lower temperatures for one of the smallest balls despite some moderate roughness.

This size-controlled kinetic variability is also evident on the Arrhenius plot (**Fig. 3B**) where these grains overall show similar behavior but with offsets from published kinetics by different extents that generally reflect their sizes. After recasting all the results to the same radius (80 μm, **Fig. 3C**), we effectively removed the effect of grain size. Because the estimated spherical-equivalent radii of the balls are far more accurate and consistent than that of the shards, we use the remaining kinetic variation within these balls as an estimate of temperature uncertainty. At observed values of $\ln(D/a^2)$ of -14 and -12 1/s, the calculated temperature ranges for the size-adjusted data are 311 ± 8 °C and 375 ± 8 °C, respectively, consistent with the variation we observe when we perform calibration of the optical pyrometer against a reference thermocouple.

2.3 Technical issues

Using affordable hardware, a single CRH analysis can be done quickly in about the same time as a conventional He analysis, and so represents a potentially routine screening tool that every thermochronology laboratory can perform. There are a few technical issues

that are important to appreciate in order to fully evaluate the data from this study. These technical concerns have implications for measurement of low-temperature kinetics (**Fig. 3B, C; Fig. 8**) and overall data precision.

The major challenge when undertaking CRH experiments is temperature measurement, especially in the low-temperature regime (i.e., < 250°C). To increase sample throughput, we measure temperature for each grain using an optical pyrometer rather than a thermocouple. The pyrometer was calibrated with a thermocouple-instrumented sample packet each day before CRH runs. However, two difficulties prevented us from obtaining highly accurate temperature measurements below ~300°C. First, at the time of sample analysis, our pyrometer had a lower measurement limit of ~198°C, which didn't allow us to begin our experiments at temperatures where the very first measurable He release occurs. Second, due to the time needed for a sample package to reach thermal equilibrium at low temperatures, we often observed (1) temperatures recorded from the pyrometer that were lower than that from the reference thermocouple, from right after laser startup until ~300 °C, both of which were lower than the scheduled linear heating ramp that was used for data reduction and (2) brief periods of higher-than-expected temperature readings (laser overshooting) during this time period. The apparent net effect of these two issues seems mostly to be lower-than-expected ^{4}He release at low temperatures that created significant non-linear trends in Arrhenius plots of Durango apatites (**Fig. 3B, C**), which have been shown to give linear trends during long heating experiments at low temperatures (Farley, 2000). We call this issue out because even after later changes to laser software and new hardware (pyrometer) we found the problem remains, though it is much improved, and so we advise caution in using our current CRH

data for fully quantitative measurement of Arrhenius parameters at the lowest temperatures. Note that this is not a significant problem because in natural samples that are not from internal shards, both alpha-ejection and diffusion profiles will lead to concave-upward Arrhenius trends at low temperatures, ruling out use of these low-temperature data for kinetic quantification in any case. It is worth noting that Farley (2000) reported lower than expected diffusivities for Durango apatite slabs that had been polished, so it is also possible that at least for the Durango balls, the lower diffusivities are the result of near-surface damage due to air abrasion.

3. Results from TAM apatite samples

We analyzed 132 single apatite grains from six rocks collected from the Cathedral Rocks vertical profile (Fitzgerald et al., 2006). For each apatite grain, we obtained its CRH ^{4}He-outgassing curve, AHe age, corrected AHe age (see section 3.4), and ^{4}He diffusion kinetics. We also use thermal histories constrained by Fitzgerald et al. (2006) from AFT data to predict AHe ages using the RDAAM model, allowing us to explore any age dispersion remaining after removing effects of varying radiation damage and grain size. These direct results are presented in this section, and raw data for the CRH runs and U-Th-Sm measurements are included in the data repository (**Table A1, A2, A3**).

3.1. AHe total-gas ages and ^{4}He-outgassing behaviors

For each of the six rock samples, at least 20 grains were analyzed by CRH, and the single-grain total-gas ages were found to be highly dispersed (**Fig. 4; Fig. 5; Data Repository – Table A1**). The intra-sample age dispersion is not surprising, given the results obtained by Fitzgerald et al. (2006) and the larger size of our data set. Except for

a few old outliers that range up to 456 ± 13 Ma, and one young outlier of 6.7 ± 0.2 Ma, these apatites have ages ranging from 27.7 ± 0.9 to 165 ± 7 Ma (see **Data Repository – Table A1**). The associated ^{4}He -outgassing curves (*df*) have a variety of forms, some similar to that predicted by simple volume diffusion, and others that are quite complex compared to theoretical behavior. The complex ^{4}He-outgassing curves are characterized by sharp gas-release spike(s), delayed gas-release at high temperatures, or frequently a combination of both. To assist description and discussion we refer to apatite grains having *df* curves characterized by smooth unimodal peaks as showing "simple" results (i.e., they passed CRH screening), and samples showing gas spikes and anomalous high-temperature release as showing "complex" behavior (i.e., they failed CRH screening).

All the analyzed apatites show either one or two gas-release peaks, where the earlier peak always occurred in the range 572 ± 45°C (unadjusted for grain size). Less than half of the apatite grains for each of the six samples survived CRH screening, and these apatites have greater consistency in gas release, with their peaks occurring at 590 ± 35 °C. In a few cases, grains that otherwise passed our criteria for CRH screening have df curves that are broader or narrower than normal and/or show peak gas-release at temperatures up to 100 °C outside the aforementioned common range (**Fig. 6; Appendix A – Fig. A.2**). The apatites that survived CRH screening lost at least 90% of their total ^{4}He between ~300 and 750°C, and their He ages are generally younger, ranging from 30.6 ± 1.3 to 56.7 ± 1.0 Ma. Apatites that failed CRH analysis show moderately or significantly complex ^{4}He -outgassing behavior and have generally older ages ranging from 33.4 ± 1.0 to >100 Ma. We also found that for each of the six samples, up to seven grains that failed CRH

369 analysis have AHe ages that are older than the AFT central ages reported by Fitzgerald
370 et al. (2006).

371 **3.2. Effects of radiation damage and grain size**

372 All of our AHe total-gas ages should be influenced by variations in radiation damage and
373 grain size to some extent. Our TAM apatite suite has a broad range from ~25 to 100 ppm
374 in effective uranium (hereafter eU; [eU] = U + 0.238Th + 0.0012Sm; Cooperdock et al.
375 (2019)), and F_T spherical-equivalent radii ranging from ~30 to 75 μm. As in the earlier
376 AHe single-grain dataset from Cathedral Rocks (Fitzgerald et al., 2006), we found no
377 obvious relationship between measured total-gas AHe age and eU or grain size for the
378 entire sample suite (**Fig. 7C, D**). However, potential age-eU and age-size relationships
379 are evident in the subset of apatites that passed CRH screening (**Fig. 7A, B**).

380 We performed forward modeling by using the thermal histories deduced from AFT data
381 (Fitzgerald et al., 2006), F_T-equivalent spherical radius, and measured eU as input for the
382 HeFTy software (Ketcham, 2005) to predict apparent ages for all of our analyzed apatites
383 using the RDAAM model. We then normalized our total-gas ages to these RDAAM ages,
384 calling the resulting ratio the RDAAM-normalization (hereafter, RDN) – samples with
385 values of 1.0 would have ages predicted from their eU, radius, and reference thermal
386 history. For each of the six samples, RDNs are still significantly dispersed (**Fig. 4B; Data**
387 **Repository – Table A1**) with RDN ages ranging from ~ 0.5 to 3. However, the apatites
388 that survived CRH screening show a narrower range of RDN (typically ~0.5 to 1.5), and
389 these ranges are even narrower when considering the RDN values for grains from
390 individual samples, such as R1, R2, and R6.

3.3. Kinetic variations

Like conventional step-heating analysis, data from CRH analysis allow for the derivation of kinetic information. Using spherical geometry, cumulative fractional loss, the time interval between measurements, and the average sample temperature over this interval, we obtained kinetics data for ^{4}He diffusion for each grain.

We do not use CRH-derived data, at least currently, for precise determination of activation energy, diffusion coefficient, or closure temperature. Rather, we only explore first-order intra-sample kinetic variations evident in the data. This is because: (1) compared to step-heating, CRH's advantage in rapid measurement is offset at very low experimental temperatures by imprecision in measurement of small gas losses, and (2) temperature measurements by optical pyrometry are subject to significant systematic offsets below ~300°C as mentioned previously. Keeping in mind our caution in extracting kinetic parameters from the lowest-temperature portions of the Arrhenius curves, the overall locations of these curves in Arrhenius space are sufficiently well defined and precise (see section 2.2.5) to allow for meaningful comparisons.

We present only the kinetics of those apatites that passed CRH screening (**Fig. 8**), however Arrhenius plots for all samples are supplied in Appendix A (**Fig. A.3**). We do this for two reasons: First, we are particularly interested in exploring intra-sample kinetic variations between different simply-behaved apatite grains. Second, owing to the fact that kinetic parameters obtained from both step-heating and CRH are sensitive to fractional loss of gas, any presence of gas spike(s), which mostly occurs at low to intermediate

412 temperatures, or a second high-temperature release component breaks the linearity and
413 in fact the justification for Arrhenius relationships.

414 We obtained a wide range of ^{4}He diffusion kinetics (**Fig. 8A**) for grains giving expected
415 results, and there is a broad correlation between their ages (total-gas age or RDN age)
416 and ^{4}He retentivity, as assessed by relative location on the Arrhenius plot after
417 normalizing for the effect of grain size (**Fig. 8B**) or normalizing for the collective effect of
418 grain size and eU (**Fig. 8C**). Among six samples (**Fig. 8C**), R1 and R2 show a clear
419 correlation between apparent ^{4}He retentivity and either total-gas age or RDN. Sample R6
420 also shows such a correlation although it does not show very much intra-sample
421 dispersion in total-gas or RDN. Kinetic data from the R6 grains show more subtle
422 variations and less spread on the Arrhenius plot relative to other samples, with the
423 exception of sample R3. Sample R3 did not show any significant intra-sample variation in
424 ^{4}He diffusion kinetics, while variations in both its total-gas age and RDN are significant.
425 Such correlation between age and kinetics is weaker in samples R4 and R5 unless the
426 oldest age in R4 (array of red points) and the youngest age in R5 (array of blue points)
427 are not included.

428 **3.4. Age correction**

429 We attempted to correct the ages of those apatites characterized by complex outgassing
430 behavior by using the peak-fitting process proposed by McDannell et al. (2018). The goal
431 of performing such age correction is not only to obtain potentially useful age data but to,
432 more importantly, to explore possible complexities in ^{4}He diffusion systematics. Based on
433 the assumption that gas released as spikes and at high temperatures are extraneous with

respect to the closure process, we started by making synthetic *df* curves using established Durango kinetics and spherical geometry in order to fit the first gas-release peak (i.e., low- to mid-temperature release of gas). This effectively removes gas spikes and/or delayed gas release at high temperatures (i.e., the second wave of gas release). We used the first peak because (1) the first peak is almost always located at or close to the temperatures at which Durango's peak gas release occurs, (2) the second peaks, if present, often appear at temperatures at or above those at which grains controlled by Durango kinetics have lost nearly all of their ^{4}He, and (3) the second peaks occur over a wide temperature range and often have broad and complex shapes. We discuss the possible complexity of the delayed gas-release further in **section 4**.

Corrected ages were calculated by stripping "extraneous" ^{4}He from the sample release using the synthetic *df* curves as a reference, and then applying the measured parent U-Th-Sm. Obviously, the ^{4}He correction will always lower ages because the correction process only removes gas component(s). We found that most of the ages from this apatite suite correct to younger than ca. 61 Ma, resulting in a much-reduced intra-sample dispersion (**Fig. 4; Fig. 5**). However, we also noted that for each sample some of the corrected ages are as young as ~20 Ma. This is considerably younger than the youngest ages obtained from grains that passed CRH screening or other studies from the area and is probably not plausible geologically (see **section 4.7**).

4. Discussion

Our results from CRH analysis of TAM apatites from the Cathedral Rocks vertical profile revealed significant intra-sample dispersion in AHe ages, and the dispersion remains

even after accounting for effects of grain size and eU. We found that the dispersion was significantly reduced by CRH screening and that the screened ages broadly correlate with kinetics. Can these observations be reconciled by a single conceptual model? Below we relate age dispersion to various types of crystal imperfections, followed by discussion of gas components, complexities in age correction, and a proposed conceptual model for ^{4}He retention.

4.1 Radiation damage: only one type of crystal imperfection

Radiation damage, from alpha decay of U and Th, introduces a range of imperfections in apatite grains that act to slow He diffusion (e.g., Gautheron et al., 2009; Flowers et al., 2009). Our results suggest that the dispersion observed in the Cathedral Rocks suite cannot be explained solely by radiation damage, therefore requiring the existence of other crystal imperfections that augment radiation damage's role in complicating He diffusion. This interpretation stems from the observation that while samples showing expected diffusion behavior do exhibit possible correlations of age with grain size and eU, they also show broad correlations between age and kinetic parameters. Additionally, crystallographic study of etched apatite grains from this sample suite reveals the presence of dislocations and sub-grain boundaries that could potentially alter kinetic parameters (**Fig. 2**).

4.2 Crystal imperfections terminology

To clarify our discussion, we first define some important terms that have had various usages in the (U-Th)/He literature. First, as used by Farley (2000), the term "defects" or "damage" refers to a broad range of crystal imperfections stemming from radiogenic and

mechanical damage that alters the kinetics of ^{4}He diffusion. In the more recent (U-Th)/He literature the term “damage” has been implicitly used as an equivalence for “radiation damage” because of the development and wide application of the RDAAM model. In order to avoid miscommunication, we will use crystal “defects” as an overarching term to refer to finer-scale imperfections and damage resulting from deformation – dislocations, sub-grain boundaries, grain boundaries, and point defects (Karato, 2008) – as well as point defects and somewhat larger features associated with radiation damage. Some of these finer-scale defects (i.e., radiation damage) have been shown to impede diffusion and have been also termed “traps”. To avoid confusion related to this usage, we prefer to use the term “sink” to refer to a broader range of probably larger imperfections such as fluid inclusions and micro-voids that might act as reversible sinks for diffusing He atoms. Owing to the fact that the term “trap” can depict both objects and processes, in this document we only use “trap” as a verb to describe processes that temporarily “store” He atoms in reversible sinks and separately use “radiation damage” when this kind of diffusion inhibition by defects is mentioned. To summarize, in our usage and discussion defects are finer-scale imperfections that slow down diffusing He atoms while “sinks” are larger imperfections that can physically trap He atoms and are possibly reversible.

4.3 Outgassing components

Probably the most obvious feature of gas release from an apatite grain that fails CRH screening is the delayed release of ^{4}He at anomalously high temperatures (above ~700 ˚C at a heating rate of 30˚C/min for typical grain sizes), which often represents a considerable fraction of the total gas and produces a second often unimodal-like gas-release peak on its *df* plot. This component of gas release might result from any types of

crystal imperfections that can act as diffusion sinks. This could include larger sinks such as fluid inclusions (Baxter, 2003), pores (Lippolt et al., 1994; Watson and Cherniak, 2003; Domingos et al., 2020), and microvoids (Zeitler et al., 2017b), but could also include smaller defects like edge dislocations that might also trap helium. These features might trap diffusing ^{4}He only temporarily, in proportion to the degree that these sinks are reversible. Small defects might anneal and return trapped helium to the lattice (Recanati et al., 2017), but for larger imperfections, the mechanism for this is not clear. Given the low solubility of He in apatite (on order 2 x 10^{-11} mol/g-bar; Zeitler et al., 2017b), it would seem difficult for any trapped He to re-enter the lattice by solution alone since the changes in pressure that would accompany laboratory heating (2-3x) would be small compared to solubilities estimated from Henry's Law. It thus seems more likely that an additional temperature-sensitive mechanism is required to get ^{4}He in sinks to return to the volume-diffusion regime in the lattice.

Another common feature of the He release from apatites that have failed CRH screening is sharp spikes of gas release at low to intermediate temperatures. These spikes can at times account for a considerable fraction of the total ^{4}He release, though generally being smaller compared to the broader secondary ^{4}He released at anomalously high temperatures. The transient nature of these spikes and their occurrence only at low to moderate laboratory temperatures suggest that they might be derived from very near-surface crystal imperfections which have trapped ^{4}He and then rupture during heating.

4.4 Evaluation of age correction

The results of our attempts at age correction lead us to question the validity of our age-correction procedure as we applied it, which in itself may provide some critical clues as to the sources of the various ^{4}He components recognized in apatites with complex ^{4}He release. We noted that age correction does not greatly reduce dispersion in these samples, but it generally shifts ages to lower values that in some cases seem far too young based on previous thermochronological results from this part of the TAM. The correction scheme based on the simple removal of ^{4}He released as spikes and at high temperatures implicitly relies on the assumption that all of these anomalous components are “extraneous” (i.e., these components are not part of the syn- and post-closure radiogenic daughter production) and therefore should be omitted for age calculation. However, this assumption is likely unfounded for reasons we elaborate below.

4.5 A conceptual ^{4}He transport model for apatite

Successful models for He accumulation and loss in apatite must be able to reconcile the observed intra-sample dispersion in AHe ages, anomalous outgassing components, and kinetic variations. Consider an apatite that acquired a blend of crystal imperfections including both defects and sinks immediately after its crystallization or perhaps later during deformation; this would almost certainly be the norm. As this apatite cooled but was still warmer than its closure temperature for ^{4}He, diffusing radiogenic ^{4}He could be trapped during its random walk in any crystal imperfection it encounters if these imperfections act as sinks at the current ambient conditions. The accumulation of this trapped early radiogenic component would be considered to be extraneous with respect to normal expectations about cooling ages. This trapping would be controlled by the density of potentially many types of sinks of various sizes. In contrast, at temperatures

below the He closure temperature diffusion would be extremely sluggish, and there would be little or no new trapping of existing or ongoing radiogenic production in sinks. Thus, natural samples with He sinks would contain radiogenic ^{4}He in two different locations: "normal" lattice sites, and sinks, with the sinks filled only with atoms that had undergone significant numbers of diffusion jumps at higher temperatures. The abundance of ^{4}He in sinks would be a function of the number of sinks present, the ability of ^{4}He to escape from sinks, and the thermal history, since slow cooling or isothermal thermal histories will permit extended intervals over which diffusing atoms could encounter a sink, in contrast to a quenched thermal history in which almost all radiogenic production would occur at lower temperatures.

When outgassing of these sink-bearing apatite crystals is undertaken in the laboratory, ^{4}He atoms that had not previously encountered a sink would begin to diffuse through the crystal, and those that did not encounter a sink on the way out would be released to define the first gas-release peak of the *df c*urve. However, ^{4}He atoms that are part of this "normal" diffusing component would also have a high probability of encountering sinks during laboratory heating. Thus, trapping could occur during two phases: for higher-temperature ^{4}He components (i.e., at temperatures above closure) that are produced or incorporated into the crystal in geologic times, and for all ^{4}He components during outgassing in the laboratory. Finally, at higher laboratory temperatures, any ^{4}He trapped in sinks, including ^{4}He that was trapped both in natural and in laboratory processes, would see a high probability of escaping to return to the volume-diffusion regime, and be manifested in the second high-temperature release peak around ~800°C. In detail, given the tortuous random-walk path taken by ^{4}He atoms as they migrate through apatite crystals, it is

568 conceivable that some ^{4}He atoms might become trapped and released multiple times,
569 depending on the kinetics of trap escape. In this model, AHe ages that are greater than
570 their AFT counterparts would be geologically meaningful.

571 Zeitler et al. (2017b) pointed out that given the large number of diffusion jumps needed
572 for an atom to escape from a crystal, the probability becomes very high that an atom will
573 encounter a feature within the lattice. This agrees with our conclusion that gas-release
574 spikes are sourced from imperfections located very near the grain surface and our
575 observation that even grains with very complex behavior show only a few such spikes.
576 Overall the number of sinks within a grain need not be very large or voluminous to
577 significantly alter diffusion systematics within a grain.

578 In this model, an age correction scheme that removes all of the laboratory high-
579 temperature gas-release would result in an underestimation of the amount of ^{4}He
580 expected from closure theory and therefore yield an overcorrected age. The degree of
581 overcorrection would be worst for a rapid-cooled sample in which almost all trapping
582 happened in the laboratory, and least for a sample taken directly from the partial retention
583 zone, for which a significant fraction of its ^{4}He found in sinks arrived there in nature.

584 What is challenging but interesting is that the ratio of low- to high-temperature gas release
585 in the laboratory is a sample-specific property that will be controlled not only by the
586 amount and type(s) of sinks but also by the thermal history. These factors will determine
587 what proportion of the ^{4}He content was geologically mobile and thus prone to trapping
588 under natural conditions. Thus, the presence of a secondary CRH release peak is most

589 directly an indication that sink-related crystal imperfections are present in the sample.
590 Whether a useful age correction scheme can be developed under this model is unclear
591 and will require further work. However, it is also worth noting that for a given sample, all
592 of the grains will have experienced the same thermal history, therefore the remaining
593 dispersion in AHe ages after accounting for grain size and radiation damage via eU
594 implies the presence of other features that have influenced the accumulation and release
595 of He. This model also presents a new possibility in AHe thermochronology in that the
596 pre- and syn- closure accumulation of extraneous ^{4}He and its laboratory release at high
597 temperatures may offer the potential to recover additional constraints on thermal history
598 (e.g., at earlier times at higher temperatures). Whether this is so will depend on
599 understanding the kinetics of imperfections in apatite, and so two targets for future
600 research are understanding the degree to which imperfections of different types and sizes
601 can anneal or not, and if not, what mechanisms nonetheless return helium to the lattice.
602 Finally, another interesting unanswered question is whether the presence of larger
603 imperfections as revealed by CRH analysis would stand as a proxy for the presence of
604 finer-scale defects that might alter diffusion kinetics but not lead to trapping.

605 **4.6 Kinetic variability beyond radiation-damage models**

606 CRH results from apatites that pass CRH screening shed light on the first-order kinetic
607 variability of ^{4}He diffusion. Arrhenius plots from simply-behaved grains show that a
608 significant range of intra-sample kinetic variability remains after grain size and eU effects
609 are taken into account (**Fig. 8**). Additionally, while we observed some modest variations
610 in the small amounts of Si and Ce present in TAM apatites (**Section 2.2.1**), these
611 variations are not likely to lead to significant variations in the kinetics of fission-track

612 annealing, nor do variations in the Cl and OH content of these fluorapatites (Barbarand
613 et al., 2003). One might infer that this limited compositional control on fission-track
614 annealing could apply to ^{4}He diffusion kinetics as well. Published results relating apatite
615 composition to changes in ^{4}He diffusivity are mixed and likely complicated by the use of
616 the FT annealing proxy Dpar. However, there is a direct correlation between apatite
617 composition and track annealing. Djimbi et al. (2015) discussed calculations showing that
618 endmember fluorapatite and chlorapatites *should* have somewhat different He diffusion
619 kinetics, however the small compositional variation observed in the TAM apatites
620 suggests that halogen content is not likely to be a significant source of the kinetic
621 variations we observed.

622 Past experimental and modeling studies have shown that He diffusivity in apatite is
623 influenced by defects in the form of fine-scale radiation damage (Flowers et al., 2009;
624 Gautheron et al., 2009; Shuster and Farley, 2009), with pristine lattices being associated
625 with much more rapid diffusion. By analogy, we would argue that the defects we observed
626 to be present in varying amounts (**Section 2.2.2**) are altering the samples' diffusion
627 kinetics to different degrees, augmenting diffusivity changes due to radiation damage.
628 This is consistent with the primary data presented by Flowers et al. (2009), in which
629 radiation damage is clearly a first-order control on retentivity but considerable scatter
630 remains that we would argue reflects the presence of other defects, the impacts of which
631 would matter particularly in settings involving slow cooling or thermal stagnation, where
632 greater single-grain age dispersion often appears (e.g., Reiners and Farley, 2001;
633 Fitzgerald et al., 2006). An important area of future research will be finding non-

destructive methods to characterize the types and sizes of imperfections present in analyzed samples.

4.7 Application of CRH screening to TAM exhumation

For the Cathedral Rocks, Fitzgerald et al. (2006) documented that relatively slow cooling through the late Cretaceous (~1 °C/m.y.) was followed by slightly more rapid cooling (< 3 °C/m.y.) as constrained by the AFT age-elevation profile and inverse thermal-history modeling. However, as discussed above, their over-dispersed AHe single-grain ages were not able to further constrain the cooling/exhumation history. A final question that remains is whether, after extensive analysis, we are able to place better constraints on the Eocene-Oligocene cooling low-temperature history for the Cathedral Rocks profile. Our samples that passed CRH screening still show considerable age dispersion, and a critical question for us is whether and how to assign thermochronologically meaningful weight to each AHe age.

We would argue that without assessment of individual-grain diffusion kinetics, the significance of thermal histories determined from the individual AHe ages is unclear. In the case of our samples, the ability of CRH analysis to screen apatites based on consistent criteria – particularly unimodal *df* curves – permits us to focus on a less dispersed subset of our data. Additional screening allows us to identify a further subset of grains with ^{4}He diffusion kinetics similar to those of Durango apatite, and all our other grains are considerably more retentive: just using the offset in diffusivity seen across samples, some might be up to 25 to 30˚C more retentive in closure temperature than

655 Durango apatite, meaning that their retentivity (i.e., temperature sensitivity) begins to
656 approach that of fission tracks in apatite.

657 If we simply focus on ages from CRH-screened grains that have kinetics close to those
658 of Durango, we do obtain better temporal constraints and more definitive evidence of a
659 faster-cooling episode in the Cenozoic (**Fig. 9, filled diamonds**). This new interpretation
660 allows us to infer that more rapid rock exhumation began at or by 35-40 Ma and is quite
661 consistent with the thermal history proposed for the Peak 1880 profile on the north side
662 of the Ferrar Glacier (**Fig. 1; Fig. 9**) where AHe dates are less dispersed. This signal has
663 been interpreted as tectonic, either due to dextral-transtension (Olivetti et al., 2013, 2018)
664 or rifting and escarpment retreat further south along the Transantarctic Mountain front
665 (Miller et al., 2010). Such increase in cooling/exhumation rate at ca. 35 Ma is also a
666 cooling/exhumation signal seen at a number of locations along the TAM, and this
667 enhanced exhumation in the Late-Eocene-early Oligocene has been alternatively
668 attributed to enhanced erosion due to the onset of glaciation in Antarctica at ~35 Ma (e.g.,
669 He et al., 2021; Thomson et al., 2019).

670 **5. Conclusions**

671 Assessment of outgassing components and evaluation of age corrections suggests that
672 ^{4}He transportation in apatite might be controlled by mechanisms that are more complex
673 than those considered in current models for the (U-Th)/He system. We argue that CRH
674 analysis can be used to empirically screen apatites for ^{4}He components trapped in a
675 variety of high-retentivity features presented in some apatite crystals (i.e., sinks), and
676 additionally permit assessment as to whether ^{4}He diffusion is occurring as expected from

existing volume diffusion and radiation-damage models. Our reinvestigation of an age-dispersed suite of apatites from the Cathedral Rocks of the TAM using CRH analysis documents the presence of such retentive ^{4}He sinks in many of the analyzed apatite grains. Screening of the results has allowed us to identify a subpopulation of the analyses comprised of the youngest cluster of the AHe ages that exhibit unimodal ^{4}He outgassing behavior and Durango-like kinetics that suggest rapid rock exhumation at *ca.* 35 Ma, consistent with other geological evidence suggesting regional initiation of glaciation at the end of the Eocene (ref. Ivany et al., 2006).

Our findings underscore the important message that simple volume diffusion and current radiation-damage models may be insufficient to fully describe (U-Th)/He systematics in some apatite populations. Experiments using CRH can characterize ^{4}He abundance and characterize ^{4}He release behavior in as little as 30 minutes per aliquot, making it suitable for routine dating. Having information such as this in hand before attempting age interpretations and modeling seems to us far more preferable than relying on statistical manipulation or analysis of numerous grains to address age dispersion after the fact. We recommend more widespread deployment of CRH as well as ^{4}He/^{3}He analysis for routine AHe dating, especially for sample suites that show significant age dispersion.

Acknowledgments

Both this work and part of HG's graduate study were supported by the National Science Foundation [grant EAR-1726350 to AKF, PKZ, and BDI]; PGF acknowledges support from the National Science Foundation [grants OPP-0002824 and OPP-9615294] for the original (U-Th)/He work along the TAM. The rock samples were originally collected as

part of Antarctic fieldwork through the Antarctic Research Centre of Victoria University of Wellington with samples originally processed by Fitzgerald at the University of Melbourne, Australia. We thank Peter Reiners, Uttam Chowdhury, and the Arizona Radiogenic Dating Laboratory for U-Th-Sm-Ca measurements. Quantitative analyses were performed on a JEOL JXA-8530FPlus electron microprobe at the University of Minnesota. Funding for electron microprobe facility used in this research was provided by NSF grant EAR-1625422. Most of the graphs were created using Generic Mapping Tools (GMT) v. 6.0 (Wessel et al., 2019). We thank Cécile Gautheron, Rich Ketcham, and an anonymous referee for helpful and constructive reviews. We thank Fred Jourdan for efficient editorial handling.

Research Data

Research Data associated with this article can be accessed via Harvard Dataverse at https://doi.org/10.7910/DVN/FWAZHT

References

Allibone A. H., Cox S. C., Graham I. J., Smellie R. W., Johnstone R. D., Ellery S. G. and Palmer K. (1993) Granitoids of the Dry Valleys area, southern Victoria Land, Antarctica: plutons, field relationships, and isotopic dating. *N. Z. J. Geol. Geophys.* **36,** 281-297.

Ault A. K., Gautheron C. and King G. E. (2019) Innovations in (U–Th)/He, fission track, and trapped charge thermochronometry with applications to earthquakes, weathering, surface-mantle connections, and the growth and decay of mountains. *Tectonics* **38,** 3705-3739.

Barbarand J., Carter A., Wood I. and Hurford T. (2003) Compositional and structural control of fission-track annealing in apatite. *Chem. Geol.* **198,** 107-137.

Baxter E. F. (2003) Quantification of the factors controlling the presence of excess 40Ar or 4He. *Earth Planet. Sci. Lett.* **216,** 619-634.

Beucher R., Brown R. W., Roper S., Stuart F. and Persano C. (2013) Natural age dispersion arising from the analysis of broken crystals: Part II. Practical application to apatite (U–Th)/He thermochronometry. *Geochim. Cosmochim. Acta* **120,** 395-416.

Brown R. W., Beucher R., Roper S., Persano C., Stuart F. and Fitzgerald P. (2013) Natural age dispersion arising from the analysis of broken crystals. Part I: Theoretical basis and implications for the apatite (U–Th)/He thermochronometer. *Geochim. Cosmochim. Acta* **122,** 478-497.

Cooperdock E. H., Ketcham R. A. and Stockli D. F. (2019) Resolving the effects of 2-D versus 3-D grain measurements on apatite (U–Th)/He age data and reproducibility. *Geochronology* **1,** 17-41.

Dalziel I. W. (1992) Antarctica; a tale of two supercontinents? *Annu. Rev. Earth Planet. Sci.* **20,** 501-526.

Djimbi D. M., Gautheron C., Roques J., Tassan-Got L., Gerin C. and Simoni E. (2015) Impact of apatite chemical composition on (U-Th)/He thermochronometry: An atomistic point of view. *Geochim. Cosmochim. Acta* **167,** 162-176.

Domingos R., Tremblay M. M., Shuster D. L. and Militzer B. (2020) Simulations and Experiments Reveal Effect of Nanopores on Helium Diffusion in Quartz. *ACS Earth Space Chem.* **4,** 1906-1912.

Elliot D. H. and Fleming T. H. (2004) Occurrence and dispersal of magmas in the Jurassic Ferrar large igneous province, Antarctica. *Gondwana Research* **7,** 223-237.

747 Farley K. A. (2000) Helium diffusion from apatite: General behavior as illustrated by
748 Durango fluorapatite. *Journal of Geophysical Research: Solid Earth* **105,** 2903-
749 2914.

750 Farley K. A., Wolf R. A. and Silver L. T. (1996) The effects of long alpha-stopping
751 distances on (U-Th)/He ages. *Geochim. Cosmochim. Acta* **60,** 4223-4229.

752 Farley K. A. (2002) (U-Th)/He dating: Techniques, calibrations, and
753 applications. *Reviews in Mineralogy and Geochemistry* **47,** 819-844.

754 Fayon A. K. and Hansen L. N. (2018) Rheology of the rheologically insignificant mineral
755 apatite. *18th International Conference on Thermochronology.*

756 Fitzgerald P. G. (2002) Tectonics and landscape evolution of the Antarctic plate since
757 the breakup of Gondwana, with an emphasis on the West Antarctic Rift System and
758 the Transantarctic Mountains. *Royal Society of New Zealand Bulletin* **35,** 453-469.

759 Fitzgerald P. G. (2001) Apatite fission track ages associated with the altered igneous
760 intrusive in Beacon sandstone near the base of CRP-3, Victoria Land Basin,
761 Antarctica. *Terra Antarctica* **8,** 585-592.

762 Fitzgerald P. G. (1992) The Transantarctic Mountains of southern Victoria Land: The
763 application of apatite fission track analysis to a rift shoulder
764 uplift. *Tectonics* **11,** 634-662.

765 Fitzgerald P. G., Baldwin S. L., Webb L. E. and O'Sullivan P. B. (2006) Interpretation of
766 (U–Th)/He single grain ages from slowly cooled crustal terranes: a case study from
767 the Transantarctic Mountains of southern Victoria Land. *Chem. Geol.* **225,** 91-120.

768 Fitzgerald P. G. and Gleadow A. J. (1988) Fission-track geochronology, tectonics and
769 structure of the Transantarctic Mountains in northern Victoria Land,
770 Antarctica. *Chemical Geology: Isotope Geoscience section* **73,** 169-198.

771 Florindo F., Wilson G. S., Roberts A. P., Sagnotti L. and Verosub K. L. (2001)
772 Magnetostratigraphy of late Eocene-early Oligocene strata from the CRP-3 core,
773 Victoria Land Basin, Antarctica. *Terra Antarctica* **8,** 599-614.

774 Flowers R. M. and Farley K. A. (2012) Apatite $^{4}He/^{3}He$ and (U-Th)/He evidence for an
775 ancient Grand Canyon. *Science* **338,** 1616-1619.

776 Flowers R. M. and Kelley S. A. (2011) Interpreting data dispersion and “inverted” dates
777 in apatite (U–Th)/He and fission-track datasets: an example from the US
778 midcontinent. *Geochim. Cosmochim. Acta* **75,** 5169-5186.

779 Flowers R. M., Ketcham R. A., Shuster D. L. and Farley K. A. (2009) Apatite (U–Th)/He
780 thermochronometry using a radiation damage accumulation and annealing
781 model. *Geochim. Cosmochim. Acta* **73,** 2347-2365.

782 Galeotti S., DeConto R., Naish T., Stocchi P., Florindo F., Pagani M., Barrett P., Bohaty
783 S. M., Lanci L. and Pollard D. (2016) Antarctic Ice Sheet variability across the
784 Eocene-Oligocene boundary climate transition. *Science* **352,** 76-80.

Gautheron C., Tassan-Got L., Barbarand J. and Pagel M. (2009) Effect of alpha-damage annealing on apatite (U-Th)/He thermochronology. *Chem. Geol.* **266,** 157-170.

Gerin C., Gautheron C., Oliviero E., Bachelet C., Djimbi D. M., Seydoux-Guillaume A., Tassan-Got L., Sarda P., Roques J. and Garrido F. (2017) Influence of vacancy damage on He diffusion in apatite, investigated at atomic to mineralogical scales. *Geochim. Cosmochim. Acta* **197,** 87-103.

Gleadow A. and Fitzgerald P. G. (1987) Uplift history and structure of the Transantarctic Mountains: new evidence from fission track dating of basement apatites in the Dry Valleys area, southern Victoria Land. *Earth Planet. Sci. Lett.* **82,** 1-14.

Gleadow A., McKelvey B. E. and Ferguson K. U. (1984) Uplift history of the Transantarctic Mountains in the Dry Valleys area, southern Victoria Land, Antarctica, from apatite fission track ages. *N. Z. J. Geol. Geophys.* **27,** 457-464.

Goodge J. W. (2020) Geological and tectonic evolution of the Transantarctic Mountains, from ancient craton to recent enigma. *Gondwana Research* **80,** 50-122.

Green P. and Duddy I. (2018) Apatite (U-Th-Sm)/He thermochronology on the wrong side of the tracks. *Chem. Geol.* **488,** 21-33.

Gunn B. M. and Warren G. (1962) *Geology of Victoria Land between the Mawson and Mulock Glaciers, Antarctica.* Trans-Antarctic Expedition Committee.

He J., Thomson S. N., Reiners P. W., Hemming S. R. and Licht K. J. (2021) Rapid erosion of the central Transantarctic Mountains at the Eocene-Oligocene transition: Evidence from skewed (U-Th)/He date distributions near Beardmore Glacier. *Earth Planet. Sci. Lett.* **567,** 117009.

Idleman B. D., Zeitler P. K. and McDannell K. T. (2018) Characterization of helium release from apatite by continuous ramped heating. *Chem. Geol.* **476,** 223-232.

Ivany L. C., Van Simaeys S., Domack E. W. and Samson S. D. (2006) Evidence for an earliest Oligocene ice sheet on the Antarctic Peninsula. *Geology* **34,** 377-380.

Karato S. (2008) *Deformation of Earth Materials: An Introduction to the Rheology of Solid Earth.* Cambridge University Press, Cambridge.

Ketcham R. A. (2005) Forward and inverse modeling of low-temperature thermochronometry data. *Reviews in mineralogy and geochemistry* **58,** 275-314.

Ketcham R. A., Carter A., Donelick R. A., Barbarand J. and Hurford A. J. (2007) Improved modeling of fission-track annealing in apatite. *Am. Mineral.* **92,** 799-810.

Ketcham R. A., Gautheron C. and Tassan-Got L. (2011) Accounting for long alpha-particle stopping distances in (U-Th-Sm)/He geochronology: refinement of the baseline case. *Geochim. Cosmochim. Acta* **75,** 7779-7791.

Krogh T. E. (1982) Improved accuracy of U-Pb zircon ages by the creation of more concordant systems using an air abrasion technique. *Geochim. Cosmochim. Acta* **46,** 637-649.

Lippolt H. J., Leitz M., Wernicke R. S. and Hagedorn B. (1994) (Uranium thorium)/helium dating of apatite: experience with samples from different geochemical environments. *Chem. Geol.* **112,** 179-191.

Long S. P., Thomson S. N., Reiners P. W. and Di Fiori R. V. (2015) Synorogenic extension localized by upper-crustal thickening: An example from the Late Cretaceous Nevadaplano. *Geology* **43,** 351-354.

McDannell K. T., Zeitler P. K., Janes D. G., Idleman B. D. and Fayon A. K. (2018) Screening apatites for (U-Th)/He thermochronometry via continuous ramped heating: He age components and implications for age dispersion. *Geochim. Cosmochim. Acta* **223,** 90-106.

McDowell F. W., McIntosh W. C. and Farley K. A. (2005) A precise ^{40}Ar–^{39}Ar reference age for the Durango apatite (U–Th)/He and fission-track dating standard. *Chem. Geol.* **214,** 249-263.

Miller S. R., Fitzgerald P. G. and Baldwin S. L. (2010) Cenozoic range-front faulting and development of the Transantarctic Mountains near Cape Surprise, Antarctica: Thermochronologic and geomorphologic constraints. *Tectonics* **29,** TC1003.

Meesters A. and Dunai T. J. (2002) Solving the production–diffusion equation for finite diffusion domains of various shapes: Part II. Application to cases with α-ejection and nonhomogeneous distribution of the source. *Chem. Geol.* **186,** 57-73.

Murray K. E., Orme D. A. and Reiners P. W. (2014) Effects of U-Th-rich grain boundary phases on apatite helium ages. *Chem. Geol.***390,** 135-151.

Olivetti V., Balestrieri M. L., Rossetti F. and Talarico F. M. (2013) Tectonic and climatic signals from apatite detrital fission track analysis of the Cape Roberts Project core records, South Victoria Land, Antarctica. *Tectonophysics* **594,** 80-90.

Olivetti V., Rossetti F., Balestrieri M. L., Pace D., Cornamusini G. and Talarico F. (2018) Variability in uplift, exhumation and crustal deformation along the Transantarctic Mountains front in southern Victoria Land, Antarctica. *Tectonophysics* **745,** 229-244.

Peyton S. L., Reiners P. W., Carrapa B. and DeCelles P. G. (2012) Low-temperature thermochronology of the northern Rocky Mountains, western USA. *Am. J. Sci.* **312,** 145-212.

Piccoli P. M. and Candela P. A. (2002) Apatite in igneous systems. *Reviews in Mineralogy and Geochemistry* **48,** 255-292.

Recanati A., Gautheron C., Barbarand J., Missenard Y., Pinna-Jamme R., Tassan-Got L., Carter A., Douville É, Bordier L. and Pagel M. (2017) Helium trapping in apatite

damage: Insights from (U-Th-Sm)/He dating of different granitoid lithologies. Chem. Geol. 470, 116-131.

Reiners P. W., Ehlers T. A., Mitchell S. G. and Montgomery D. R. (2003) Coupled spatial variations in precipitation and long-term erosion rates across the Washington Cascades. *Nature* **426,** 645-647.

Reiners P. W., Ehlers T. A. and Zeitler P. K. (2005) Past, present, and future of thermochronology. *Reviews in Mineralogy and Geochemistry* **58,** 1-18.

Reiners P. W. and Farley K. A. (2001) Influence of crystal size on apatite (U–Th)/He thermochronology: an example from the Bighorn Mountains, Wyoming. *Earth Planet. Sci. Lett.* **188,** 413-420.

Reiners P. W. and Nicolescu S. (2006) Measurement of parent nuclides for (U-Th)/He chronometry by solution sector ICP- MS. In *ARHDL Report 3.0 ed*.. University of Arizona.

Shuster D. L., Flowers R. M. and Farley K. A. (2006) The influence of natural radiation damage on helium diffusion kinetics in apatite. *Earth Planet. Sci. Lett.* **249,** 148-161.

Shuster D. L. and Farley K. A. (2009) The influence of artificial radiation damage and thermal annealing on helium diffusion kinetics in apatite. *Geochim. Cosmochim. Acta* **73,** 183-196.

Smellie J. L. (2001) History of Oligocene erosion, uplift and unroofing of the Transantarctic Mountains deduced from sandstone detrital modes in CRP-3 drillcore, Victoria Land Basin, Antarctica. *Terra Antarctica* **8,** 481-490.

Spiegel C., Kohn B., Belton D., Berner Z. and Gleadow A. (2009) Apatite (U–Th–Sm)/He thermochronology of rapidly cooled samples: the effect of He implantation. *Earth Planet. Sci. Lett.* **285,** 105-114.

Thomson S. N., Reiners P. W., He J., Hemming S. R. and Licht K. (2019) New constraints on the pre-glacial and glacial uplift and incision history of the central Transantarctic Mountains using multiple low-temperature thermochronometers. *AGU Fall Meeting***,** C14B-04.

Toraman E., Teyssier C., Whitney D. L., Fayon A. K., Thomson S. N. and Reiners P. W. (2014) Low-temperature thermochronologic record of Eocene migmatite dome emplacement and late Cenozoic landscape development, Shuswap core complex, British Columbia. *Tectonics* **33,** 1616-1635.

Watson E. B. and Cherniak D. J. (2003) Lattice diffusion of Ar in quartz, with constraints on Ar solubility and evidence of nanopores. *Geochim. Cosmochim. Acta* **67,** 2043-2062.

Wessel P., Luis J. F., Uieda L., Scharroo R., Wobbe F., Smith W. and Tian D. (2019) The generic mapping tools version 6. *Geochem. Geophys. Geosyst.* **20,** 5556-5564.

Willett C. D., Fox M. and Shuster D. L. (2017) A helium-based model for the effects of radiation damage annealing on helium diffusion kinetics in apatite. *Earth Planet. Sci. Lett.* **477,** 195-204.

Wilson G. S., Roberts A. P., Verosub K. L., Florindo F. and Sagnotti L. (1998) Magnetobiostratigraphic chronology of the Eocene—Oligocene transition in the CIROS-1 core, Victoria Land margin, Antarctica: Implications for Antarctic glacial history. *Geological Society of America Bulletin* **110,** 35-47.

Wolf R. A., Farley K. A. and Silver L. T. (1996) Helium diffusion and low-temperature thermochronometry of apatite. *Geochim. Cosmochim. Acta* **60,** 4231-4240.

Zeitler P. K., Herczeg A. L., McDougall I. and Honda M. (1987) U-Th-He dating of apatite: A potential thermochronometer. *Geochim. Cosmochim. Acta* **51,** 2865-2868.

Zeitler, P. K., Brown R. and Hackspacher P. (2017a), Better tools for tracing the thermal history of rocks. *Eos **98**,* doi:10.1029/2017EO073479.

Zeitler P. K., Enkelmann E., Thomas J. B., Watson E. B., Ancuta L. D. and Idleman B. D. (2017b) Solubility and trapping of helium in apatite. *Geochim. Cosmochim. Acta* **209,** 1-8.

Figure Captions

Figure 1. (A) Simplified map of southern Victoria Land showing location of the two vertical sampling profiles from Peak 1880 and Cathedral Rocks. Filled areas are ice-free. TAM: Transantarctic Mountains. (B and C) Composite AFT and AHe plots summarizing the preferred cooling/exhumation path (dashed line) for the two vertical profiles but with AHe data moved down in elevation relative to the AFT data based on the difference in closure temperatures (30 – 35 °C) divided by the geologically constrained paleogeothermal gradient (20 – 25 °C/km). Modified from Fitzgerald et al. (2006). See that paper for a detailed explanation. For the AHe data, Fitzgerald et al. (2006) judged that younger AHe ages (between the minimum age and a weighted mean) were more likely to constrain a "true" thermal history, perhaps an early precursor to using screened CRH-screened ages (as shown in this study, section 4.7). Less dispersion in the Peak 1880 AHe data allowed constraints to be placed on Late Eocene cooling, whereas much greater dispersion in AHe data from Cathedral Rocks precluded such constraints.

Figure 2. Photomicrographs of annealed, polished apatite grains etched in 0.5M HNO3, showing large range of imperfection densities and types. Long straight features are polishing scratches.

Figure 3. Incremental ^{4}He release (*df*) curves (A), and CRH-derived Arrhenius relationships (B) of Durango apatites under a 30 ˚C/min heating ramp rate. Gray curves and circles depict results from Durango shards; blue curves and triangles show results from Durango balls. Red dashed line marks diffusion kinetics of ^{4}He in Durango apatite acquired by Farley (2000) via step-heating, adjusted to a radius of 80 μm. (C) Arrhenius plot of the same analyses adjusted to a common spherical-equivalent radius of a = 80 μm in order to assess precision in the kinetics obtained by CRH, indirect verification of temperature control. (D) shows the temperature uncertainties at two points for CRH analysis of Durango balls.

Figure 4. Single-grain AHe ages (upper plot) and RDAAM-normalized relative ages (lower plot). Ages from each sample are presented in individual panels. Each plot includes measured single-grain total-gas age, screened age, and CRH-corrected age, accompanied by their kernel density estimations (KDEs). For better visualization ages older than 100 Ma were omitted, so were the age/RDAAM greater than 3; n represents numbers of plotted data points; Table A1 shows information for all ages. See text for discussion of different age types show here and in Figure 5.

Figure 5. Cathedral Rocks AHe and AFT age-elevation plots summarizing results and interpretations from this study and from Fitzgerald et al. (2006). Light blue circles and curves show single-grain total-gas AHe ages (this study) and their KDE, respectively; dark blue circles and shaded curves show single-grain screened AHe ages (this study) and their KDE; pink shaded curves show KDE of single-grain CRH-corrected ages; red circles show AHe weighed mean ages (Fitzgerald et al., 2006); orange triangles show AFT central ages (Fitzgerald et al., 2006); red dashed line shows the best-fit trend to the weighted mean AHe ages from Fitzgerald et al. (2006).

Figure 6. *df* curves measured using a 30 ˚C/min ramped heating schedule. Results from each sample are presented in individual subpanels. (A) Results from grains that passed CRH screening. (B) Results from grains that failed screening. (C) Results from all grains, color-coded into three groups: blue, grains whose AHe ages are not older than the oldest screened age in that sample; red, grains whose AHe ages are older than the fission-track central ages measured by Fitzgerald et al. (2006); orange, grains whose ages fall between the other two groups.

Figure 7. (A) Relationships between single-grain AHe age and grain size (total compilation shown in panel C). (B) Relationships between single-grain AHe age and equivalent uranium (eU) (total compilation shown in panel D). Sizes are calculated as F_T -equivalent spherical radius. To be consistent with prior publications eU is calculated as U + 0.235*Th; Cooperdock et al (2019) provide a more accurate update). Filled circles show grains that passed CRH screening.

Figure 8. CRH-derived Arrhenius relationships of apatite grains that passed CRH screening, showing relationship between AHe ages and apparent ^{4}He diffusivity. (A) Observed kinetics color-coded by observed age. (B) Kinetics adjusted to 80 μm radius, color-coded by observed age. (C) Kinetics adjusted to 80 μm radius, color-coded by RDAAM-normalized relative age. Dashed green line shows the kinetics of ^{4}He diffusion in Durango apatites measured by Farley (2000). Vertical dotted line provides visual reference to aid comparison of diffusivity variations at 10000/K = 15 (~393.5 ˚C).

Figure 9. Composite AFT and AHe plot (constructed as Figure 1C) summarizing our updated cooling/exhumation path for the Cathedral Rocks locality. Preferred path for Peak 1880 is from Fitzgerald et al. (2006).

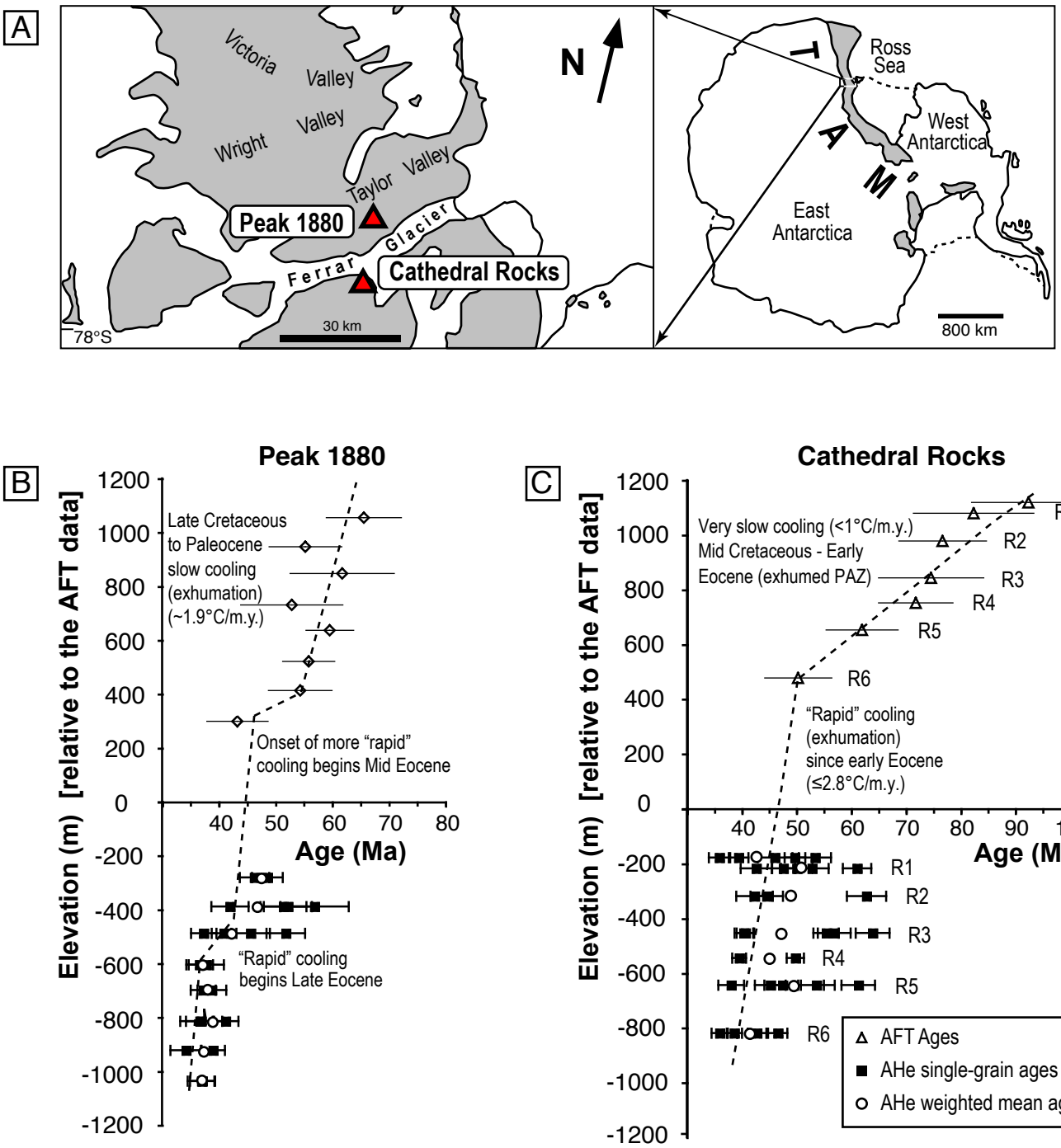
A
Victoria
Valley
Wright
Valley
Taylor
Valley
Peak 1880
Glacier
Ferrar
Cathedral Rocks
30 km
78°S
N
Ross
Sea
West
Antarctica
TAM
East
Antarctica
800 km
B
Peak 1880
Elevation (m) [relative to the AFT data]
Late Cretaceous
to Paleocene
slow cooling
(exhumation)
(~1.9°C/m.y.)
Onset of more "rapid"
cooling begins Mid Eocene
"Rapid" cooling
begins Late Eocene
Age (Ma)
C
Cathedral Rocks
Very slow cooling (<1°C/m.y.)
Mid Cretaceous - Early
Eocene (exhumed PAZ)
"Rapid" cooling
(exhumation)
since early Eocene
(≤2.8°C/m.y.)
R1
R2
R3
R4
R5
R6
AFT Ages
AHe single-grain ages
AHe weighted mean age

Figure. 1

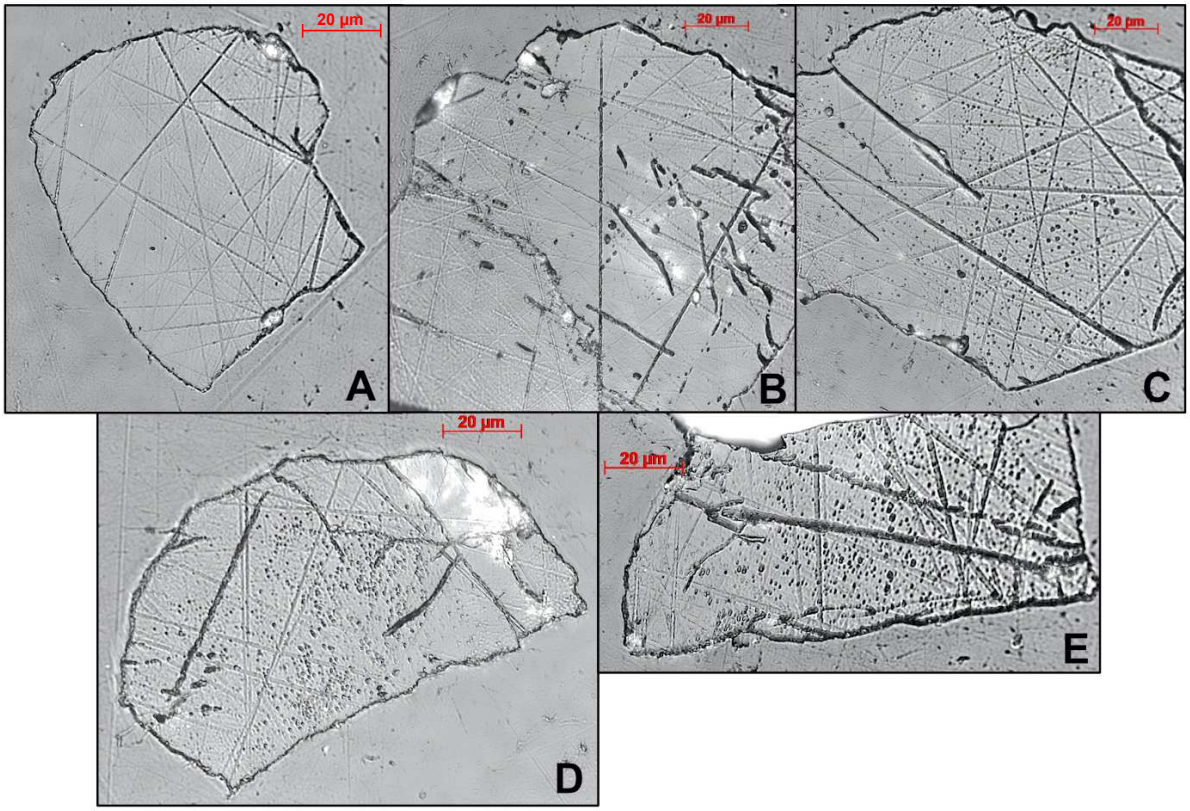

Figure 2

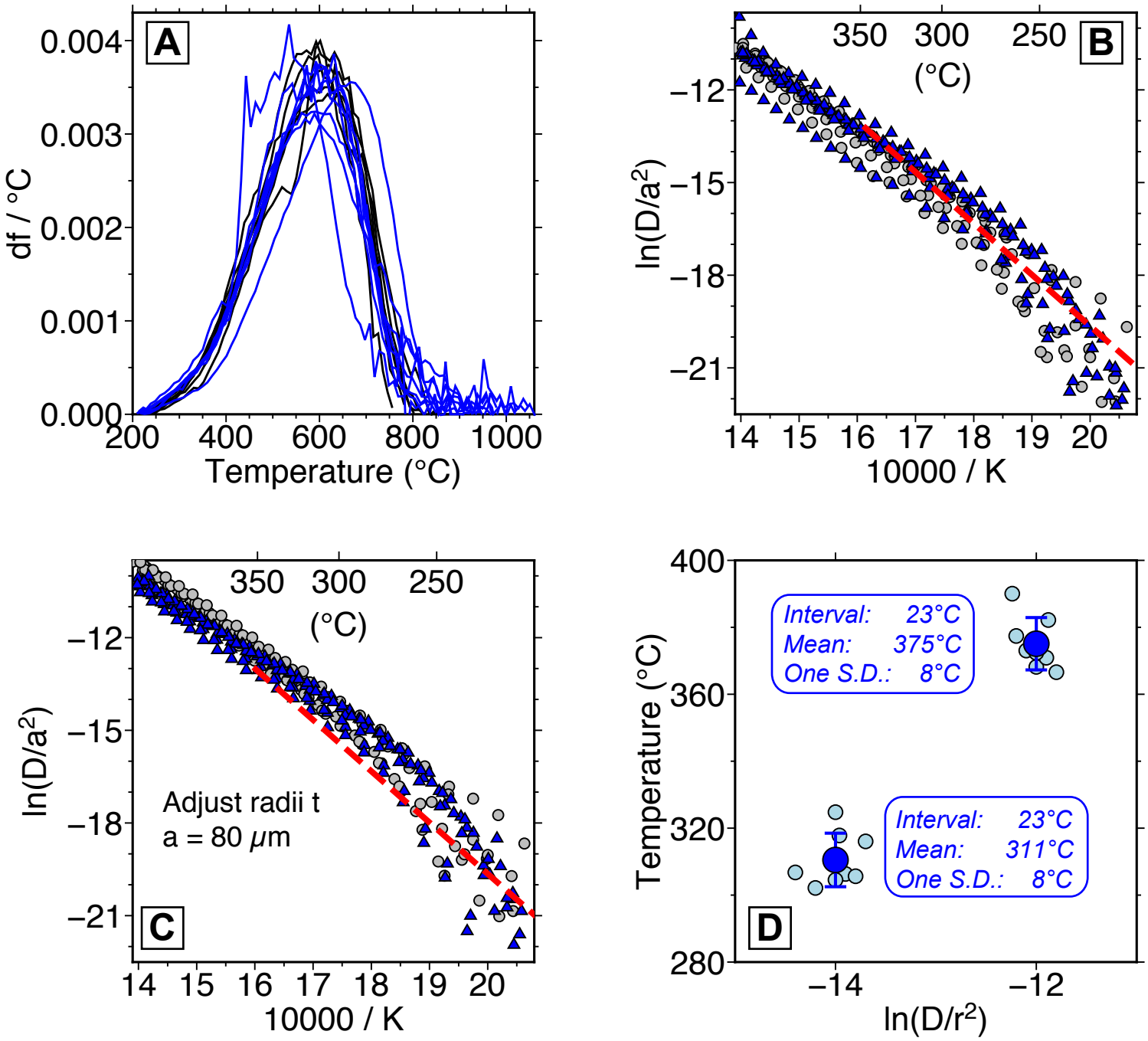
A
0.004
0.003
0.002
0.001
0.000
df / °C
200
400
600
800
1000
Temperature (°C)
B
350
300
250
(°C)
−12
−15
−18
−21
ln(D/a²)
14
15
16
17
18
19
20
10000 / K
C
350
300
250
(°C)
−12
−15
−18
−21
ln(D/a²)
Adjust radii t
a = 80 μm
14
15
16
17
18
19
20
10000 / K
D
400
360
320
280
Temperature (°C)
Interval: 23°C
Mean: 375°C
One S.D.: 8°C
Interval: 23°C
Mean: 311°C
One S.D.: 8°C
−14
−12
ln(D/r²)

Figure 3

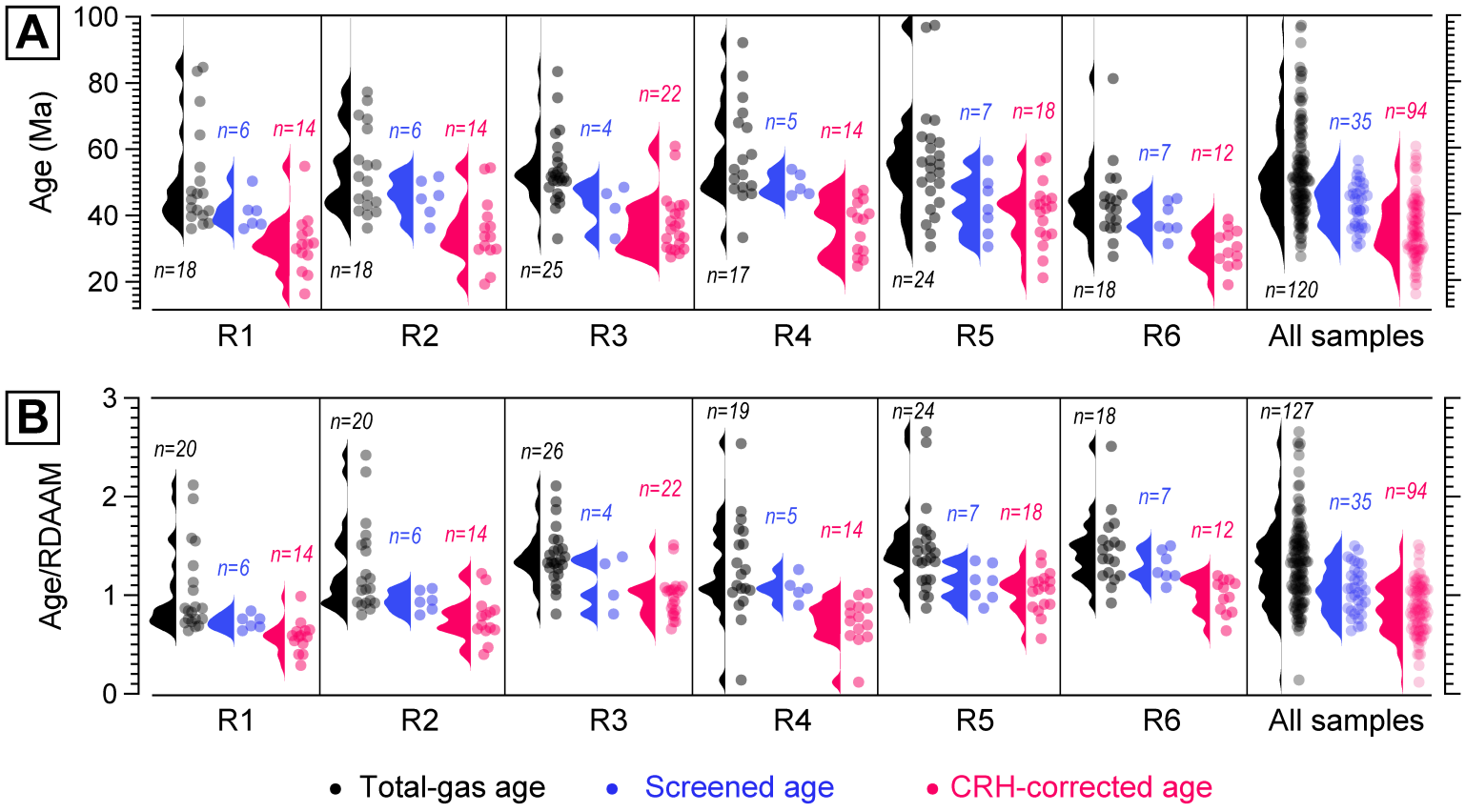
A
Age (Ma)
100
80
60
40
20
n=18
n=6
n=14
n=18
n=6
n=14
n=25
n=4
n=22
n=17
n=5
n=14
n=24
n=7
n=18
n=18
n=7
n=12
n=120
n=35
n=94
R1
R2
R3
R4
R5
R6
All samples
B
Age/RDAAM
3
2
1
0
n=20
n=6
n=14
n=20
n=6
n=14
n=26
n=4
n=22
n=19
n=5
n=14
n=24
n=7
n=18
n=18
n=7
n=12
n=127
n=35
n=94
R1
R2
R3
R4
R5
R6
All samples
Total-gas age
Screened age
CRH-corrected age

Figure 4

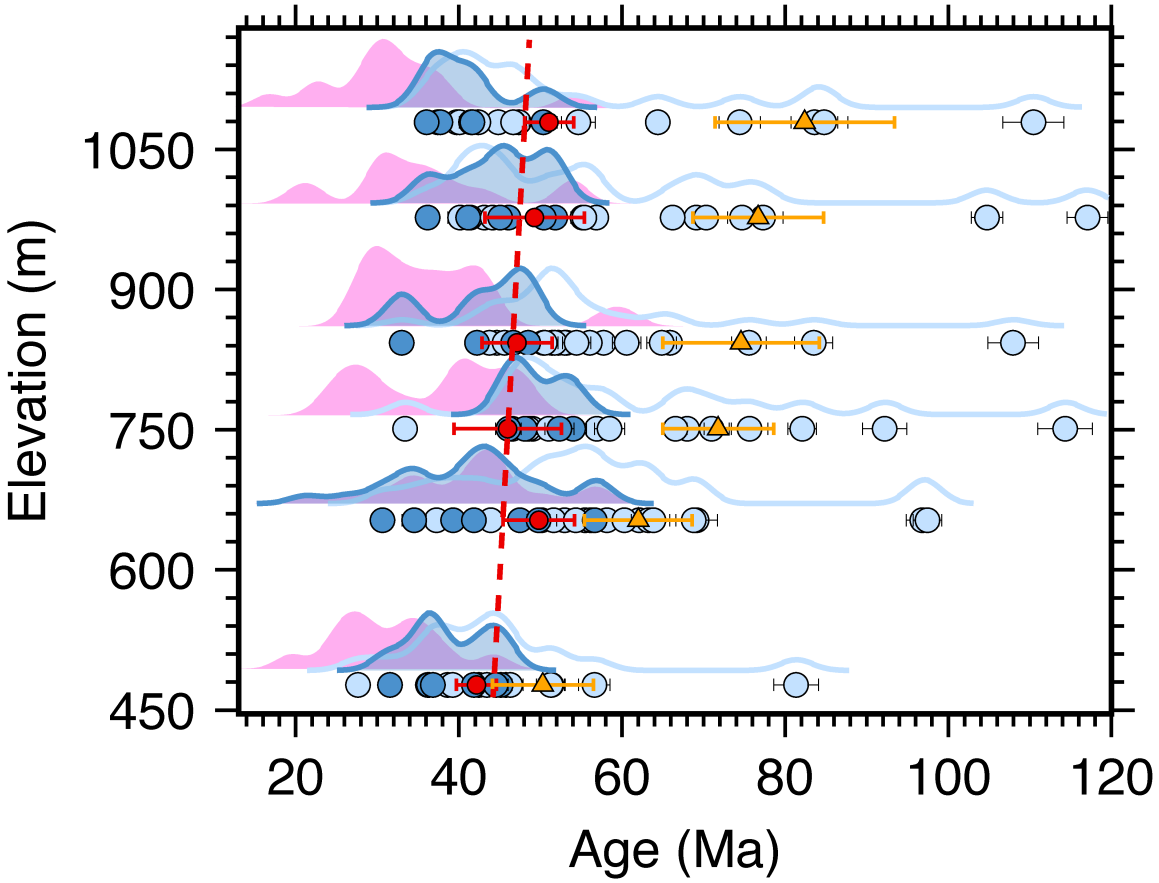

Figure 5

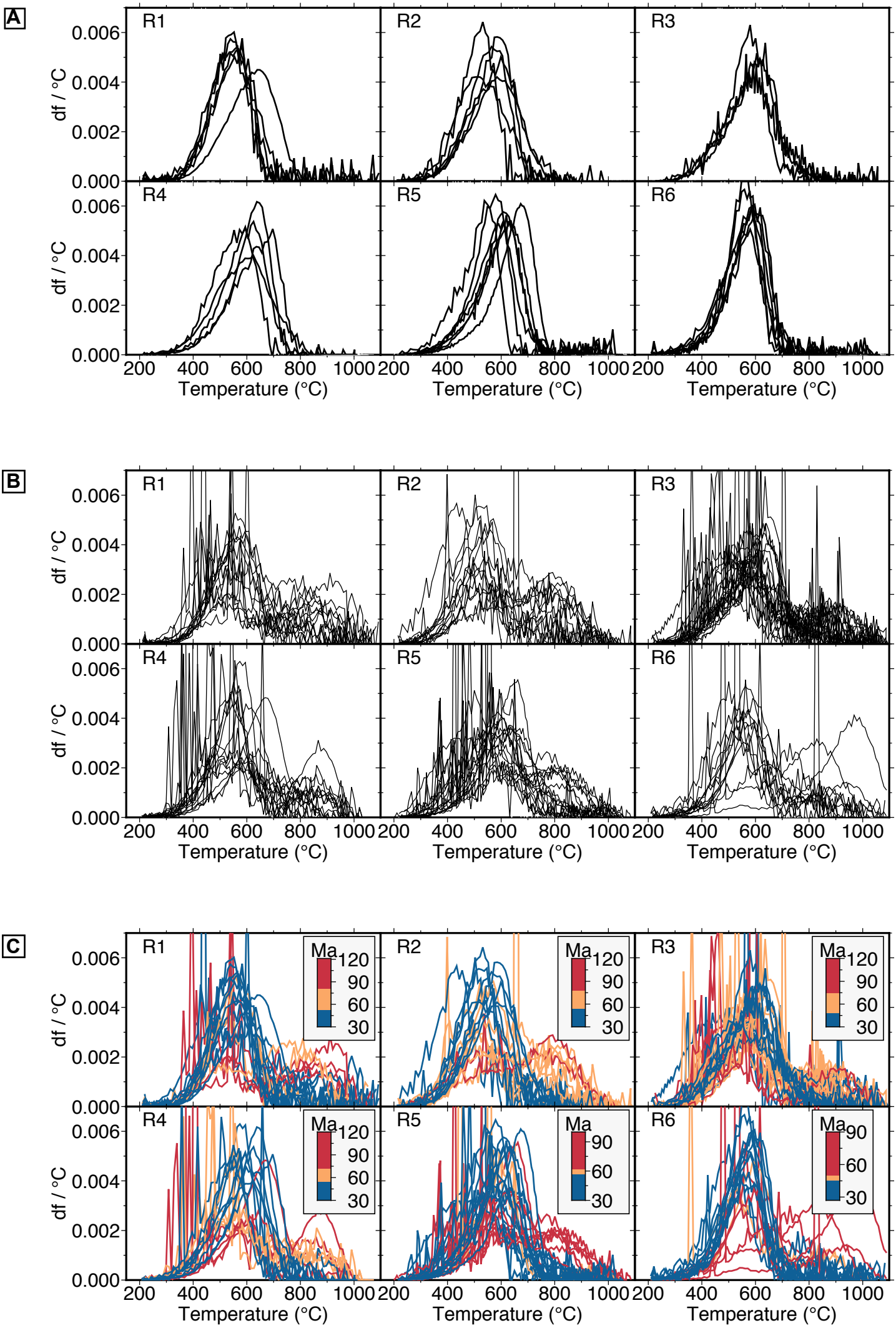
A
B
C
R1
R2
R3
R4
R5
R6
df / °C
0.000
0.002
0.004
0.006
200
400
600
800
1000
Temperature (°C)
Ma
120
90
60
30

Figure 6

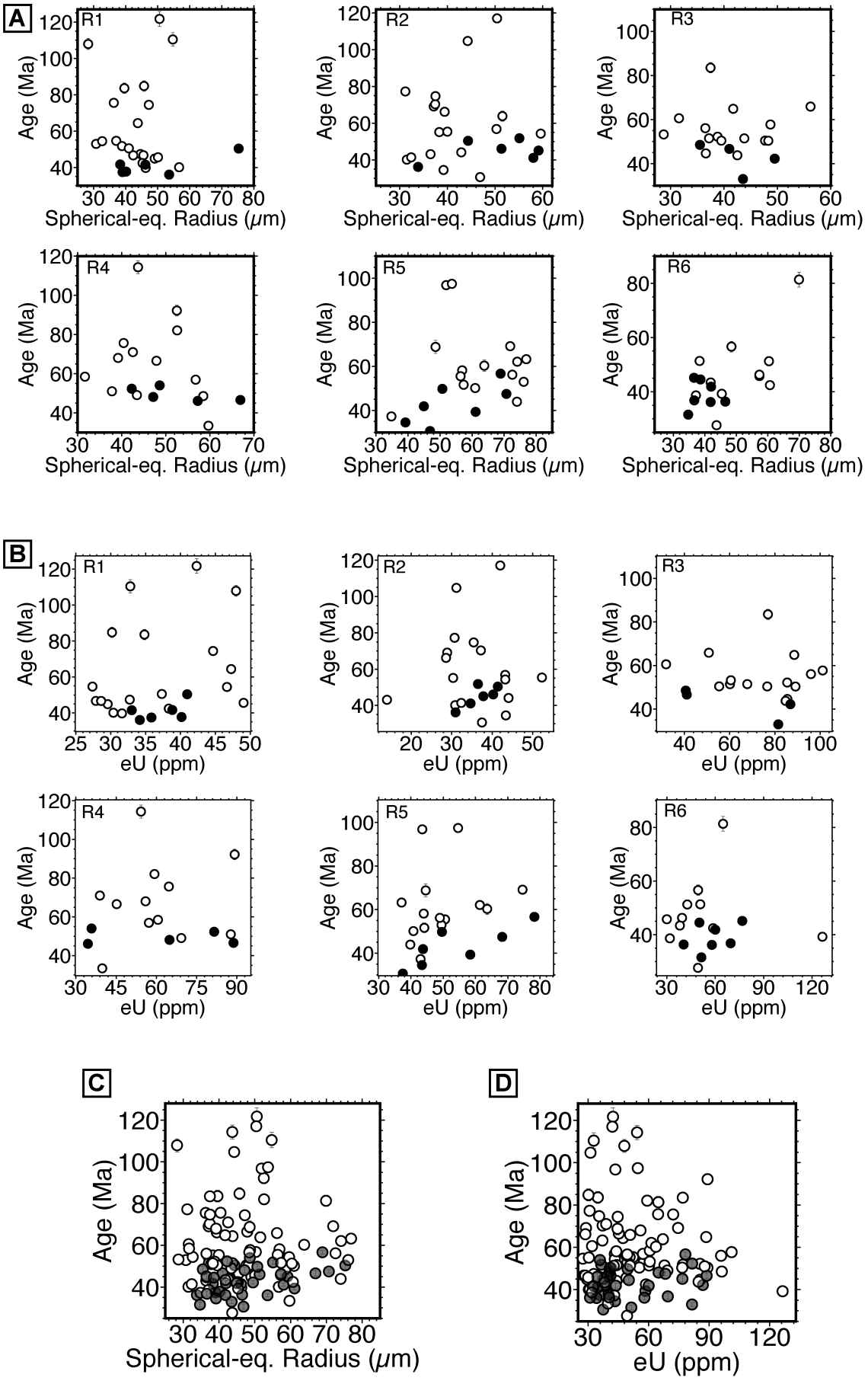

Figure 7

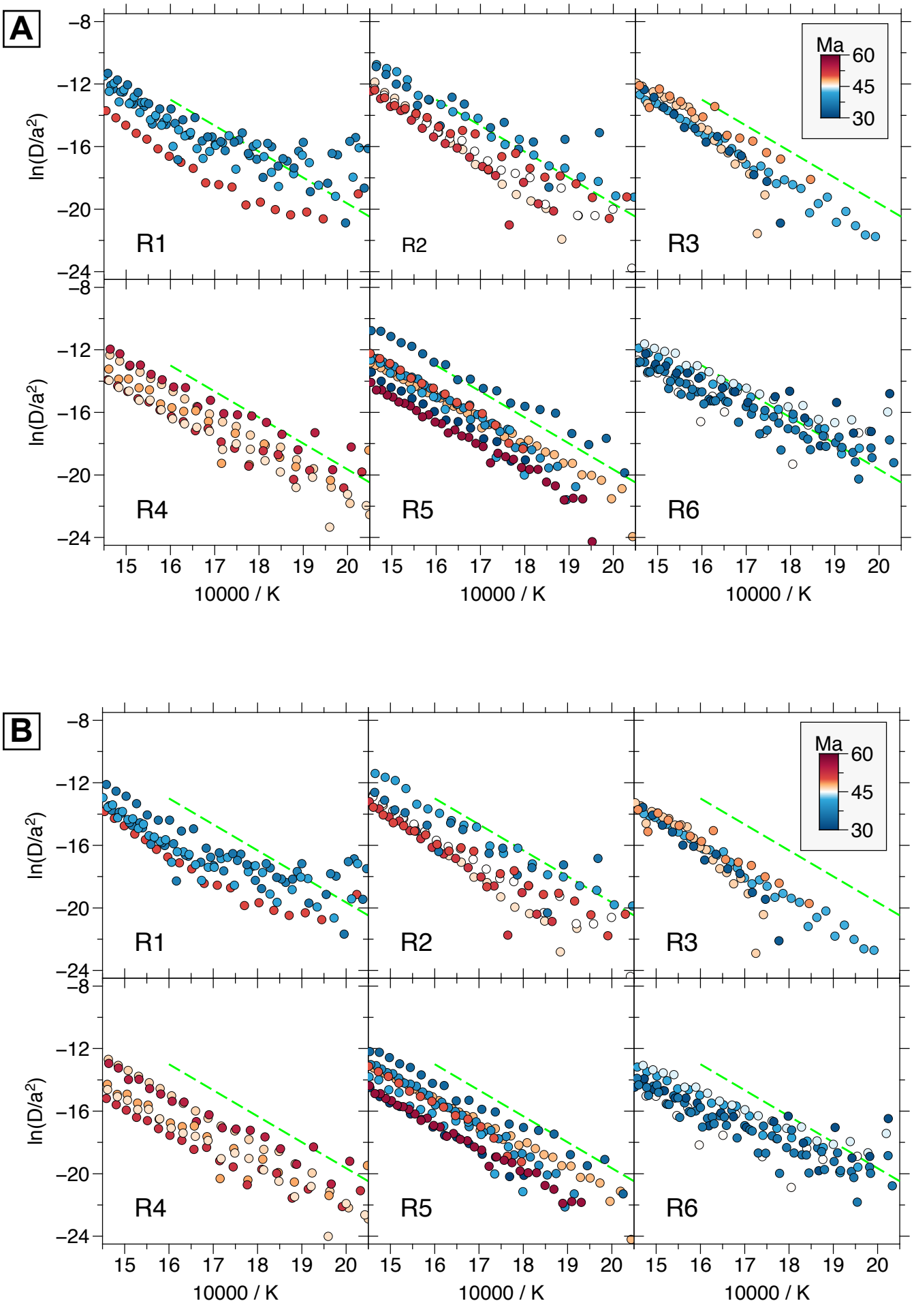
A
B
Ma
60
45
30
R1
R2
R3
R4
R5
R6
ln(D/a²)
10000 / K
−8
−12
−16
−20
−24
15
16
17
18
19
20

Figure 8

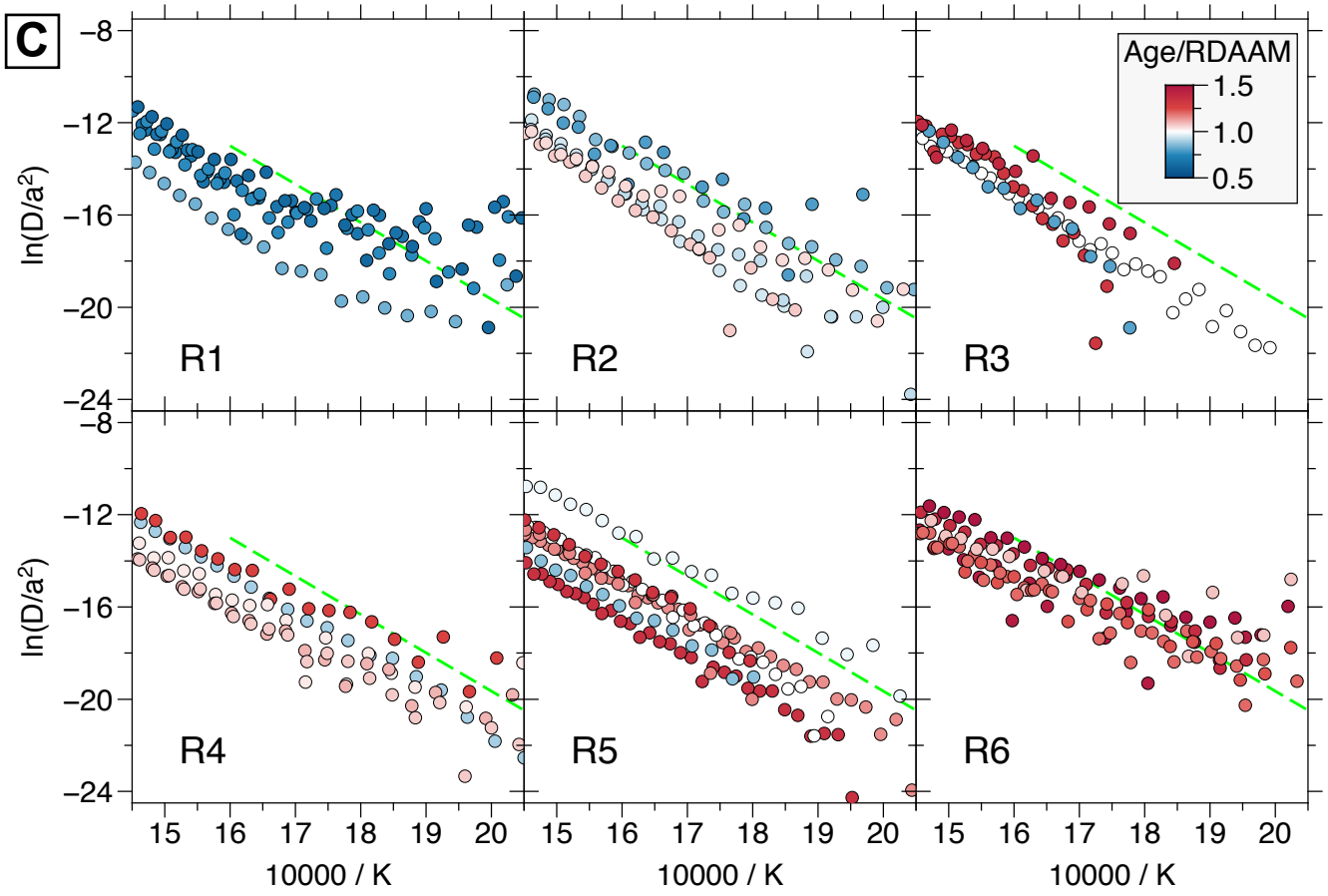

Figure 8 - continued

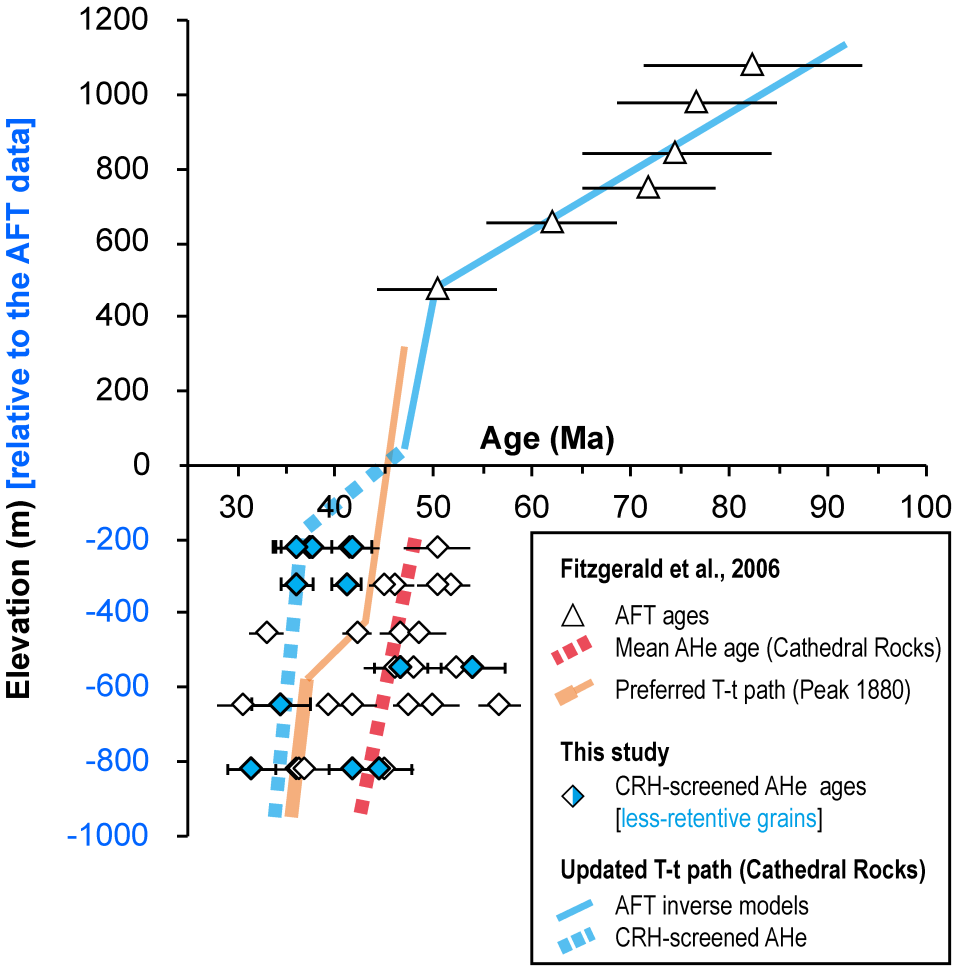
Elevation (m) [relative to the AFT data]
1200
1000
800
600
400
200
0
-200
-400
-600
-800
-1000
Age (Ma)
30
40
50
60
70
80
90
100
Fitzgerald et al., 2006
AFT ages
Mean AHe age (Cathedral Rocks)
Preferred T-t path (Peak 1880)
This study
CRH-screened AHe ages
[less-retentive grains]
Updated T-t path (Cathedral Rocks)
AFT inverse models
CRH-screened AHe

Figure 9

Appendix A: Supplementary figures with captions.

Figure A1. Ternary plot showing that compositions of TAM apatites are close to endmember fluorapatite, with little variation and minimal chlorine content. Points are color-coded according to rmr0 value (fission-track annealing parameter).

Figure A2. *df* curves for all samples. Large panels represent CRH analyses of each samples, in which the sub-plots represent single-grain CRH analyses. In each sub-plot, the single-grain sample name is marked at the upper left corner, and the single-grain total-gas age, CRH-corrected age, RDAAM-normalization, and RDAAM-normalized CRH-corrected age are listed at the upper right corner, respectively.

Figure A3. Arrhenius plots for all samples. Large panels represent Arrhenius plots of each samples, in which the sub-plots represent single-grain Arrhenius plots. In each sub-plot, the single-grain sample name, total-gas age, effective uranium, and Ft-equivalent spherical radius are listed at the upper right corner, respectively.

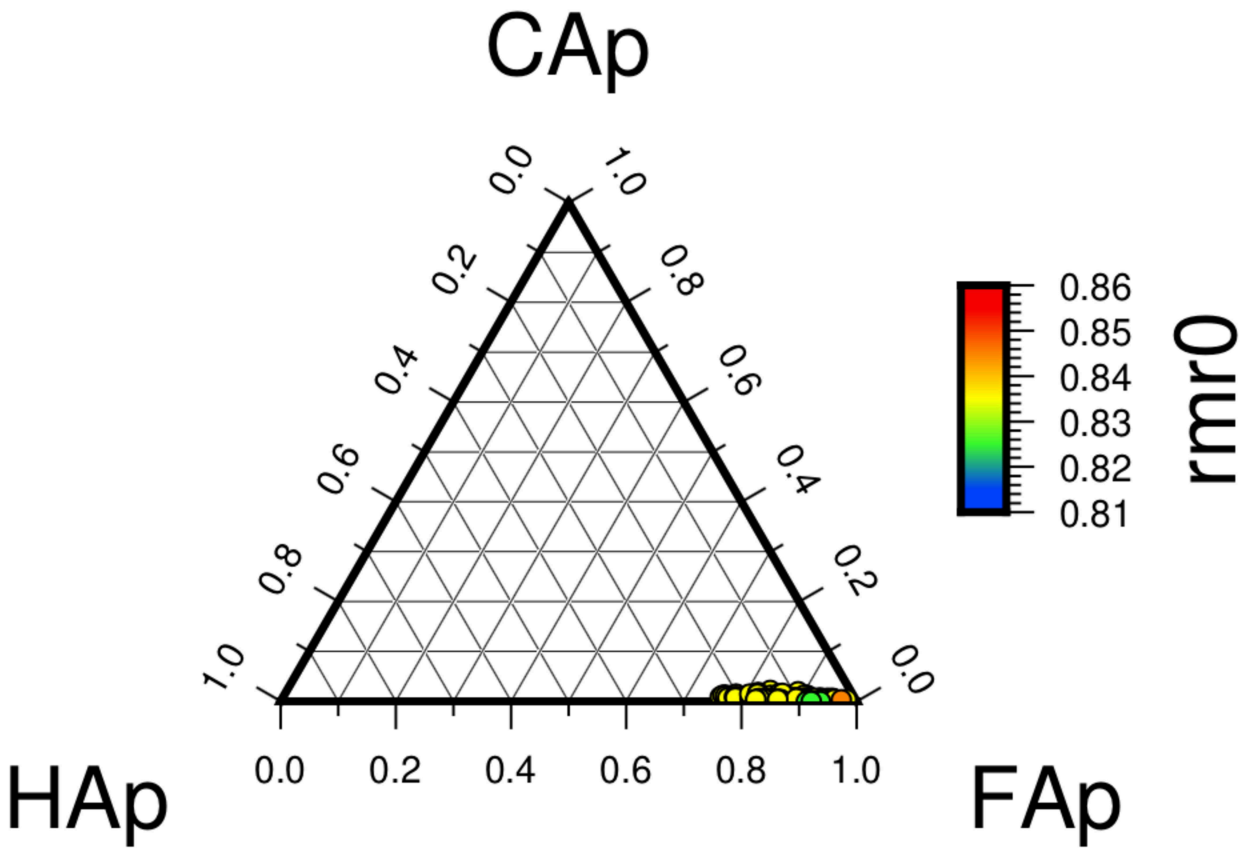

Figure A.1

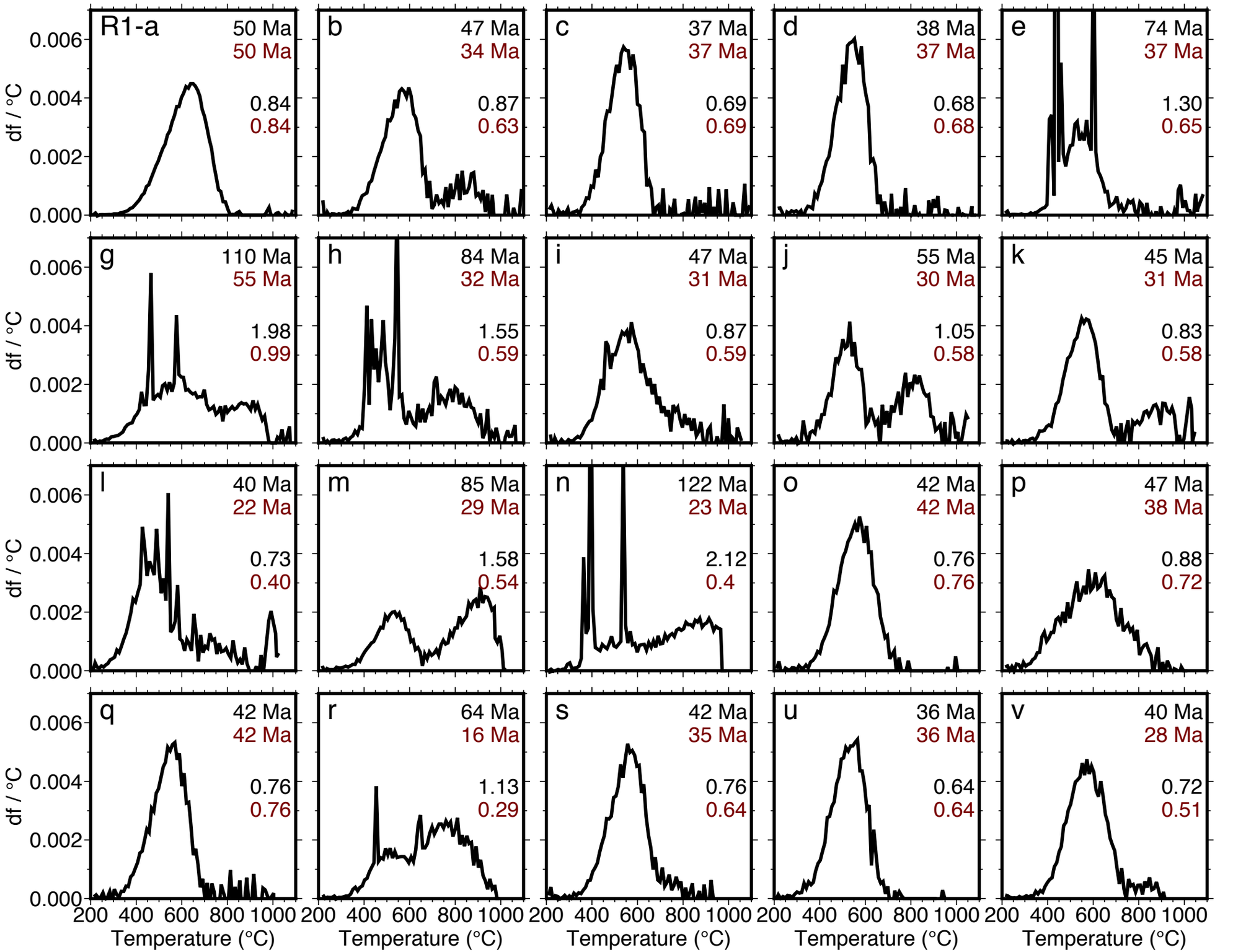
R1-a
50 Ma
50 Ma
0.84
0.84
b
47 Ma
34 Ma
0.87
0.63
c
37 Ma
37 Ma
0.69
0.69
d
38 Ma
37 Ma
0.68
0.68
e
74 Ma
37 Ma
1.30
0.65
g
110 Ma
55 Ma
1.98
0.99
h
84 Ma
32 Ma
1.55
0.59
i
47 Ma
31 Ma
0.87
0.59
j
55 Ma
30 Ma
1.05
0.58
k
45 Ma
31 Ma
0.83
0.58
l
40 Ma
22 Ma
0.73
0.40
m
85 Ma
29 Ma
1.58
0.54
n
122 Ma
23 Ma
2.12
0.4
o
42 Ma
42 Ma
0.76
0.76
p
47 Ma
38 Ma
0.88
0.72
q
42 Ma
42 Ma
0.76
0.76
r
64 Ma
16 Ma
1.13
0.29
s
42 Ma
35 Ma
0.76
0.64
u
36 Ma
36 Ma
0.64
0.64
v
40 Ma
28 Ma
0.72
0.51
df / °C
0.000
0.002
0.004
0.006
200 400 600 800 1000
Temperature (°C)

Figure A.2

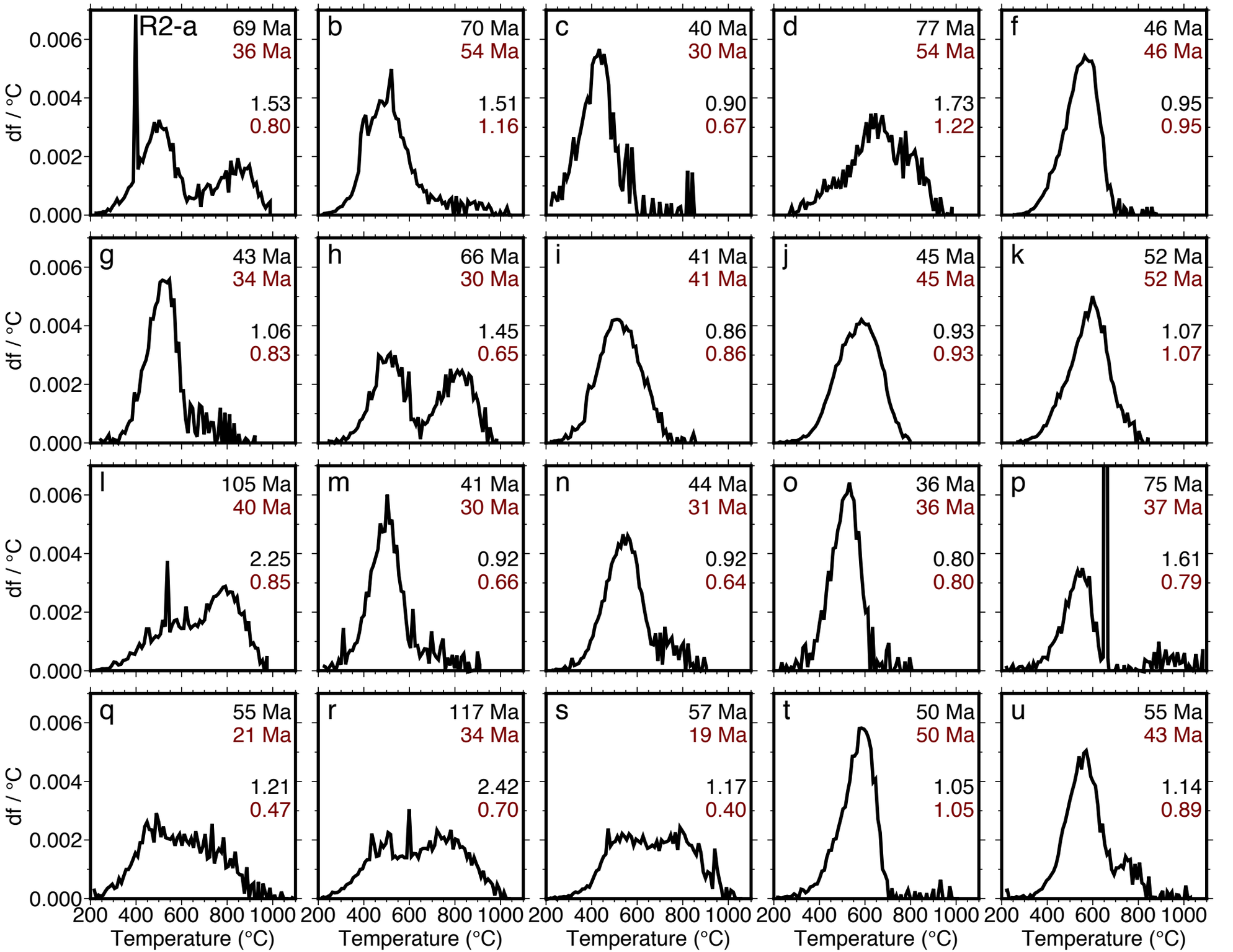

Figure A.2 - continued

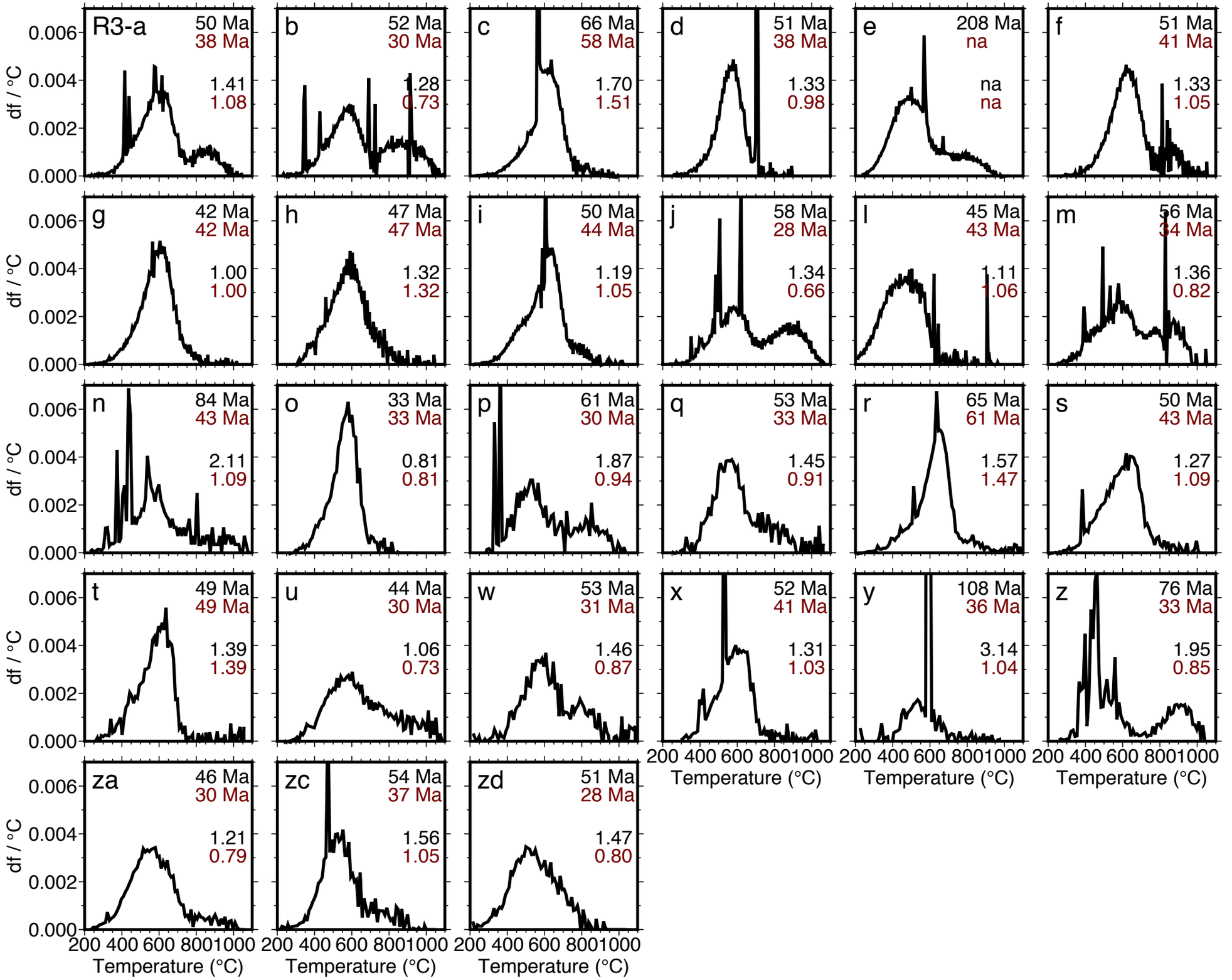

Figure A.2 - continued

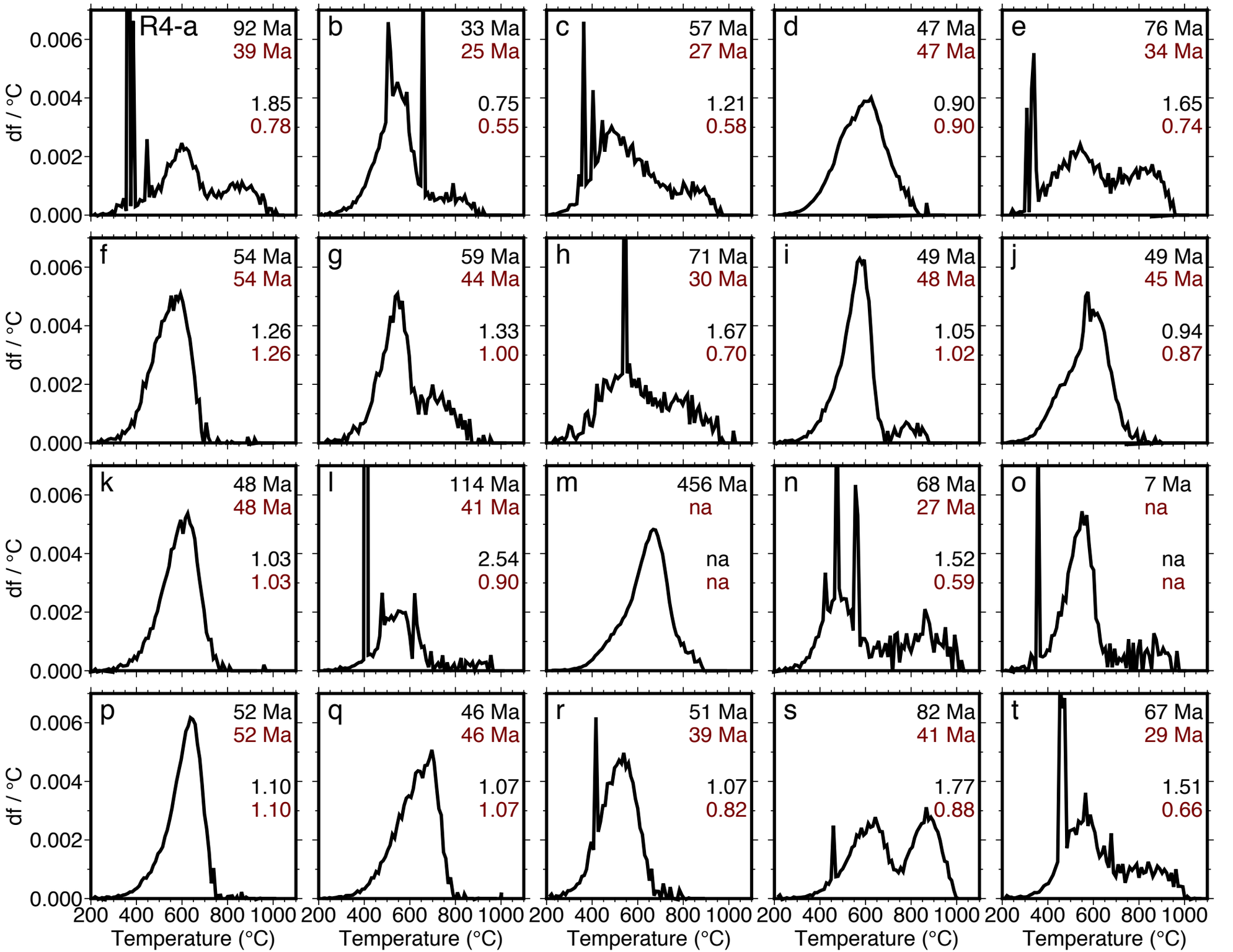

Figure A.2 - continued

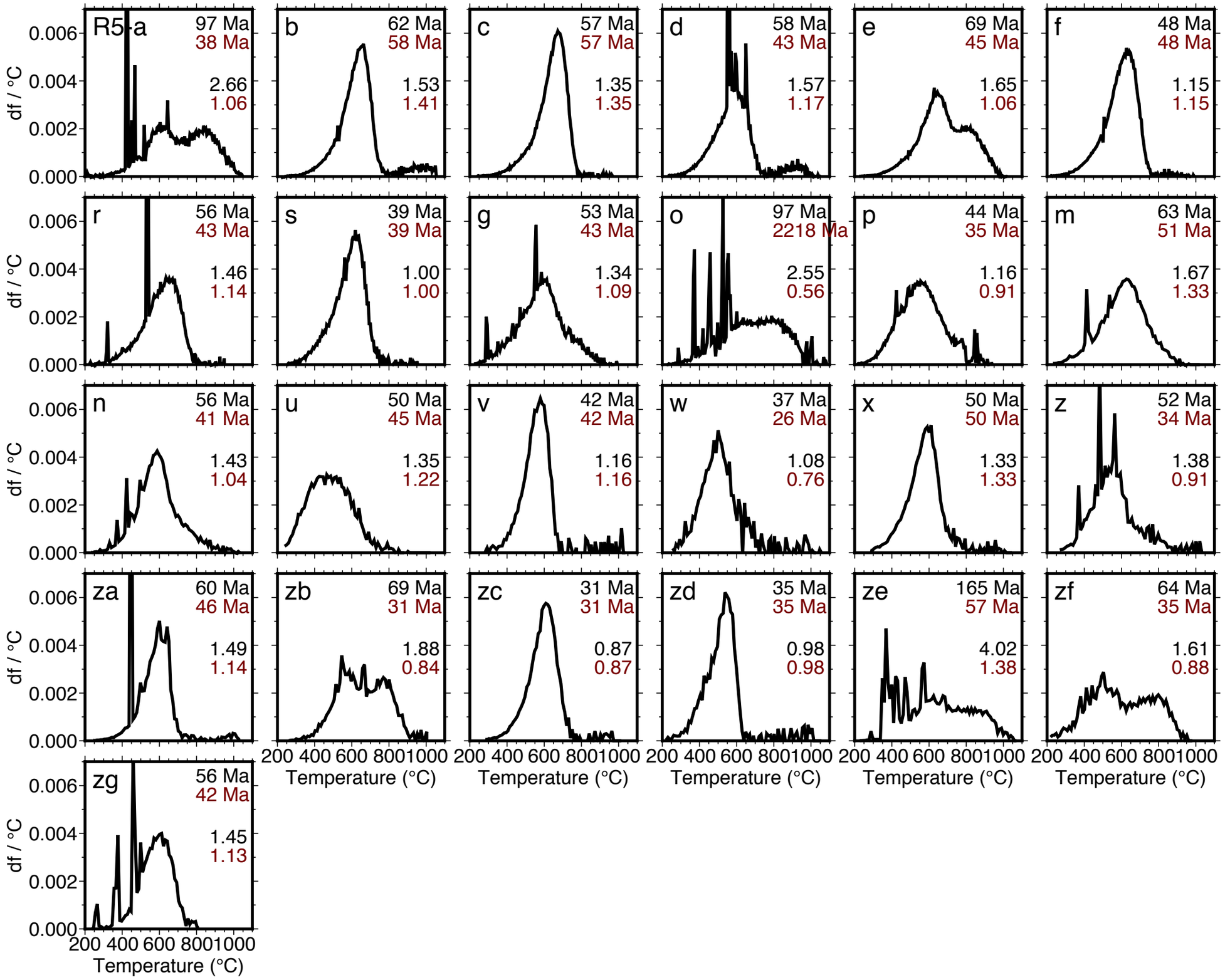

Figure A.2 - continued

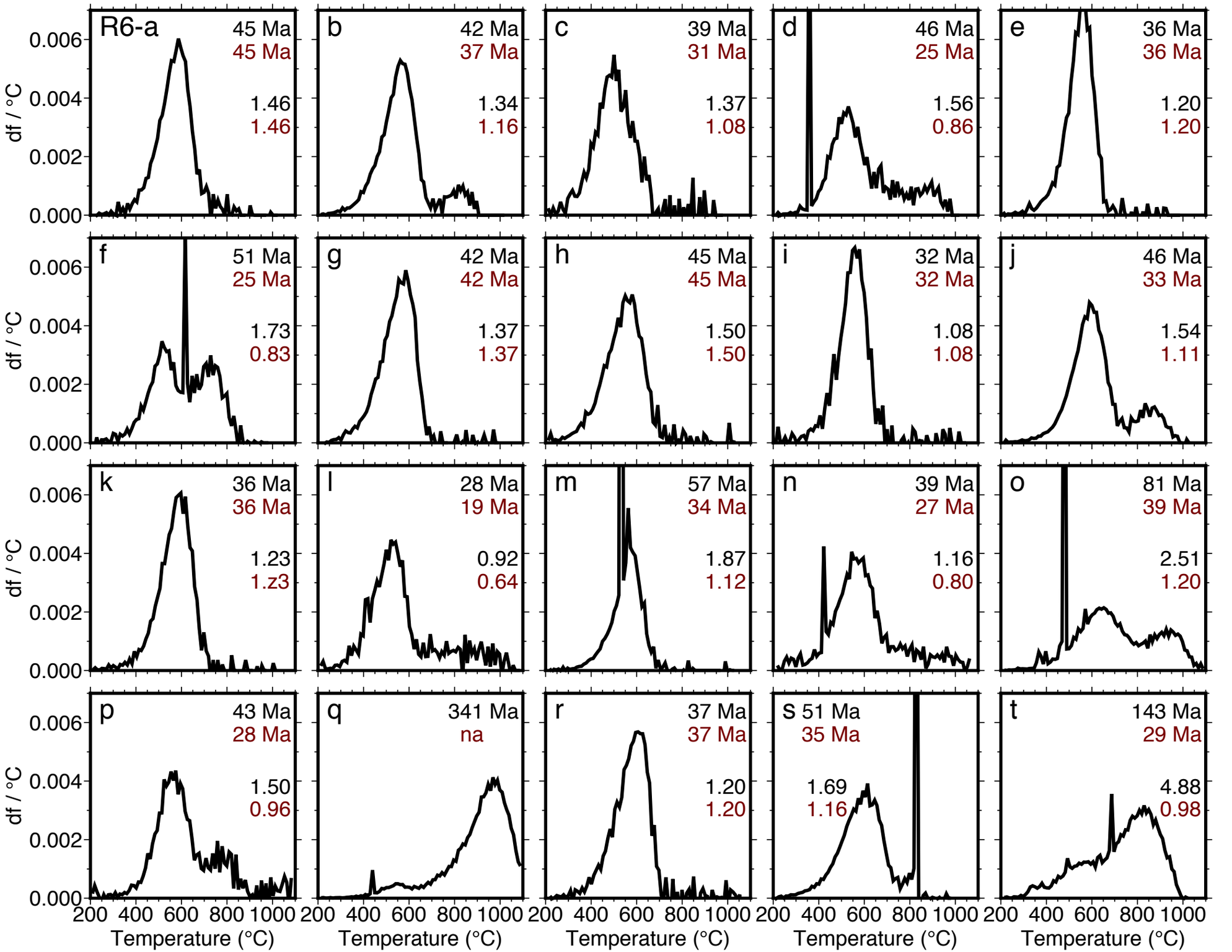

Figure A.2 - continued

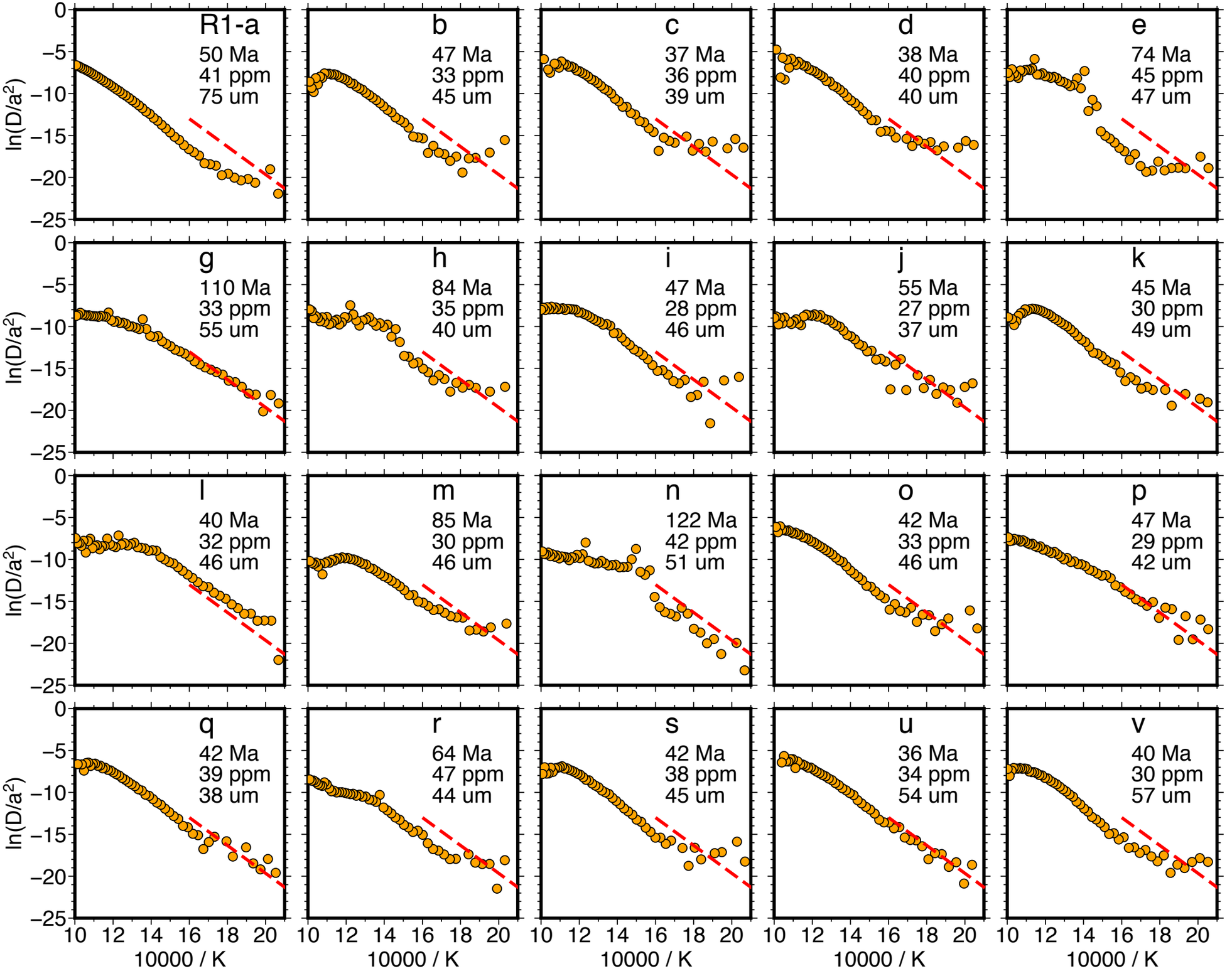
R1-a
50 Ma
41 ppm
75 um
b
47 Ma
33 ppm
45 um
c
37 Ma
36 ppm
39 um
d
38 Ma
40 ppm
40 um
e
74 Ma
45 ppm
47 um
g
110 Ma
33 ppm
55 um
h
84 Ma
35 ppm
40 um
i
47 Ma
28 ppm
46 um
j
55 Ma
27 ppm
37 um
k
45 Ma
30 ppm
49 um
l
40 Ma
32 ppm
46 um
m
85 Ma
30 ppm
46 um
n
122 Ma
42 ppm
51 um
o
42 Ma
33 ppm
46 um
p
47 Ma
29 ppm
42 um
q
42 Ma
39 ppm
38 um
r
64 Ma
47 ppm
44 um
s
42 Ma
38 ppm
45 um
u
36 Ma
34 ppm
54 um
v
40 Ma
30 ppm
57 um
ln(D/a²)
0
−5
−10
−15
−20
−25
10 12 14 16 18 20
10000 / K

Figure A.3

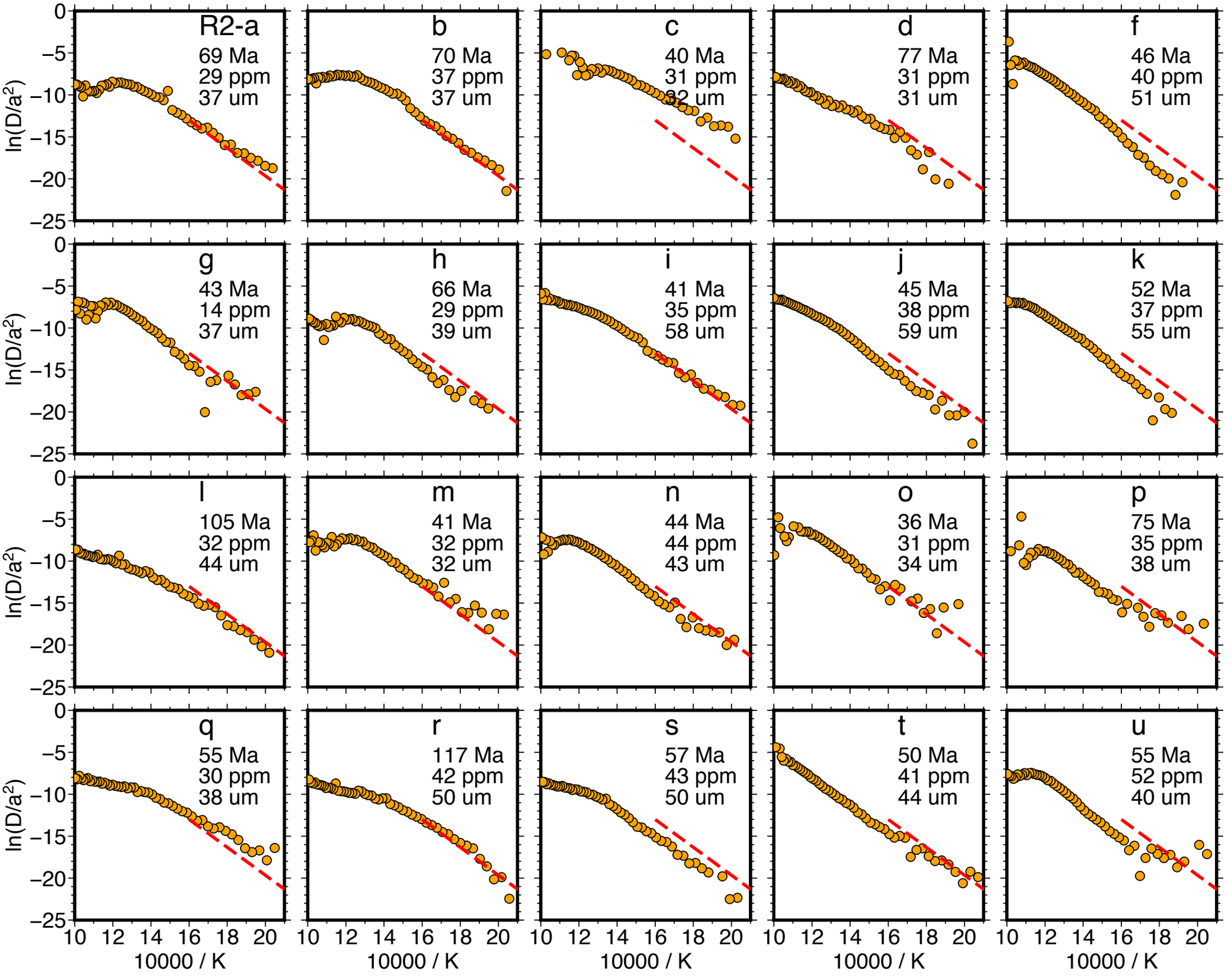

Figure A.3 - continued

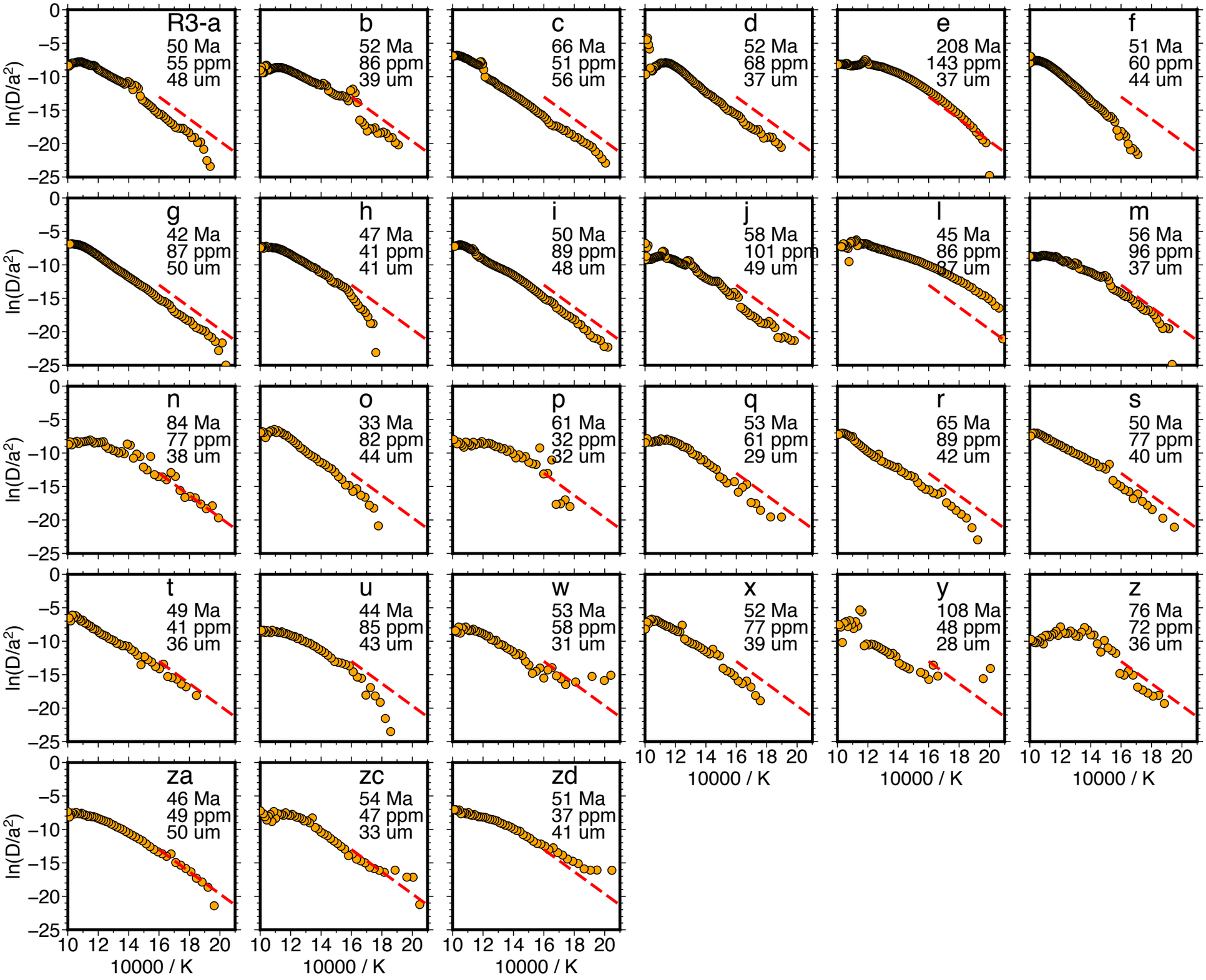

Figure A.3 - continued

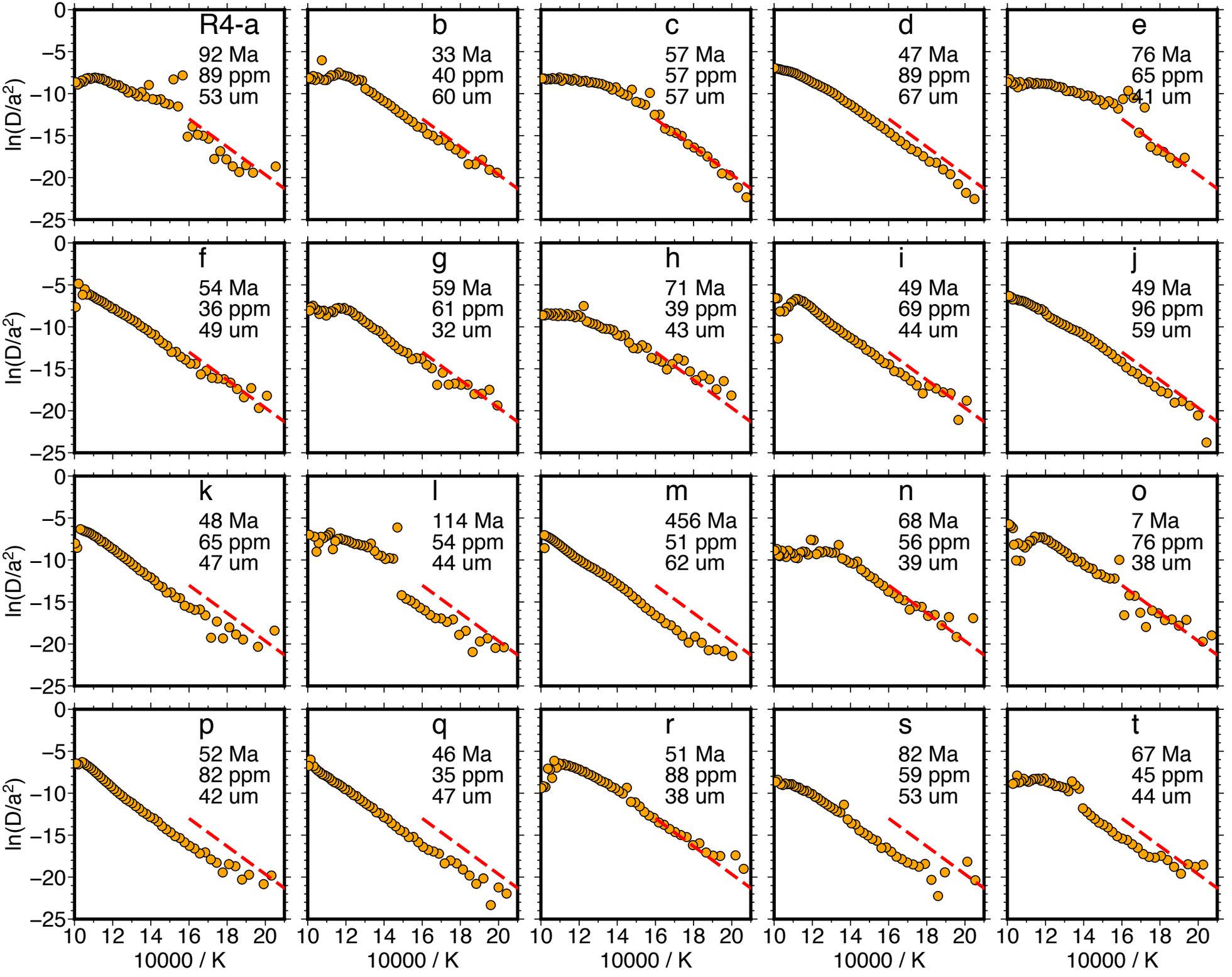

Figure A.3 - continued

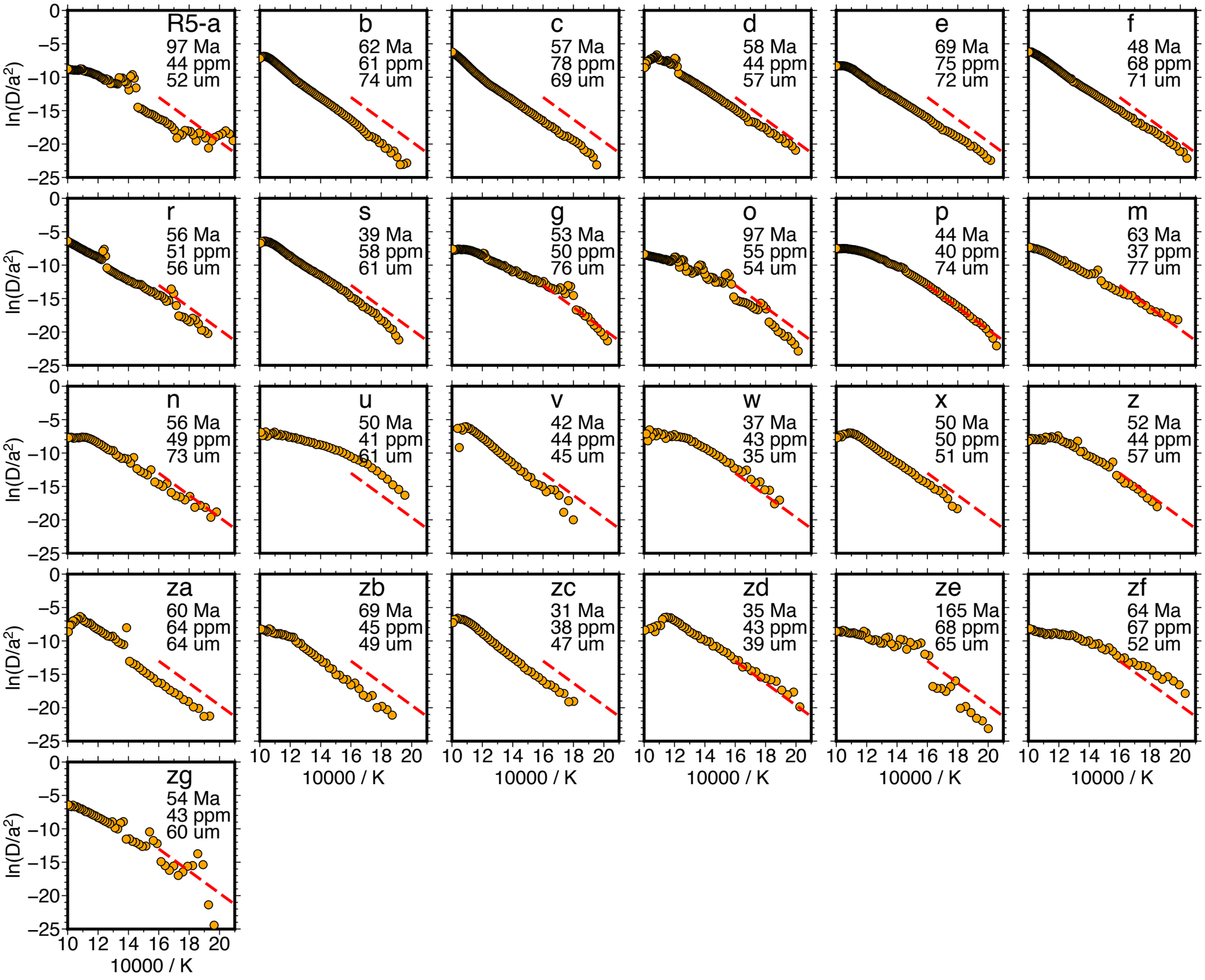

Figure A.3 - continued

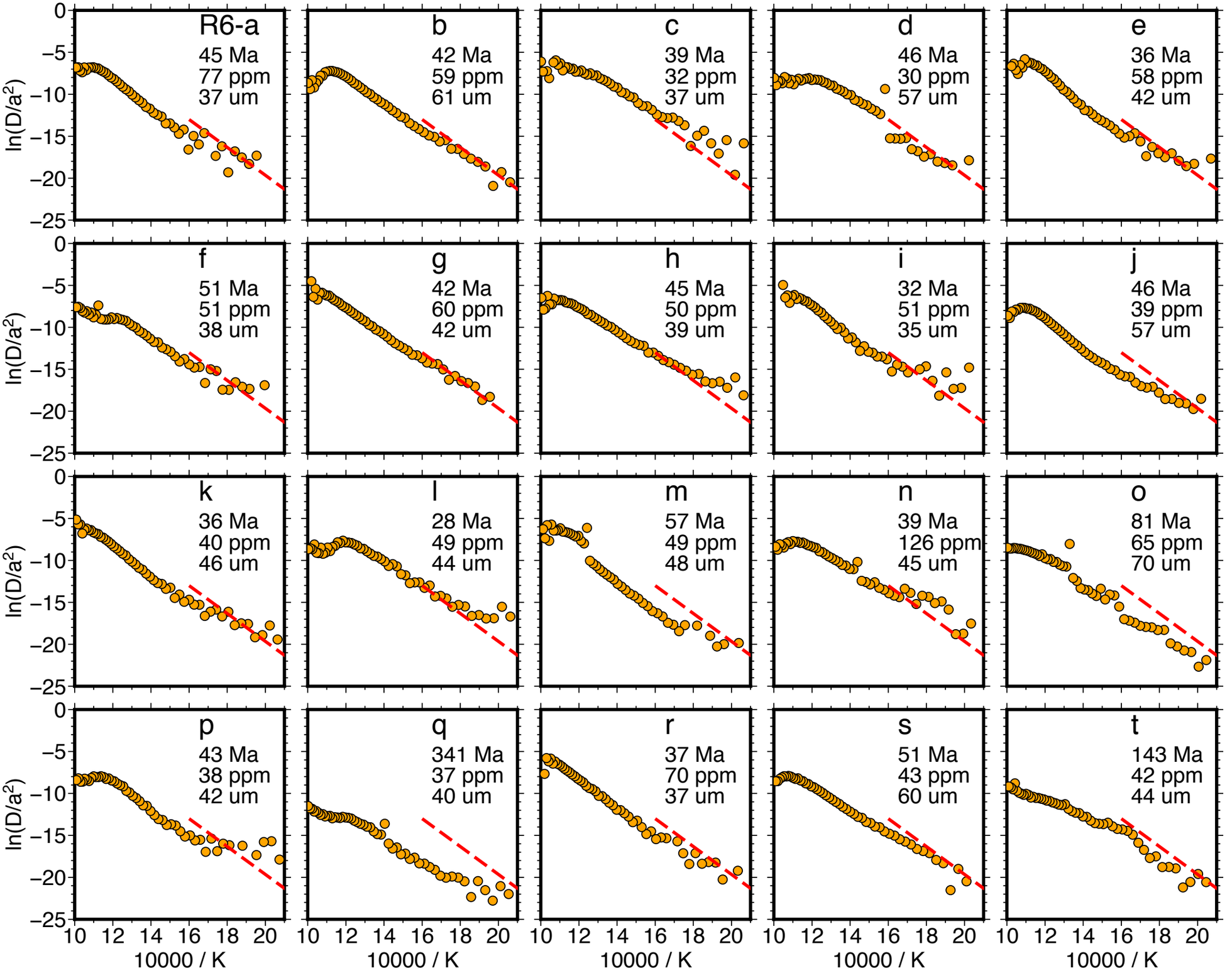

Figure A.3 - continued

Appendix B: Documentation of key procedures for continuous ramped heating

Details of the main analytical approach to Continuous Ramped Heating (CRH) can be found in Idleman et al. (2018). In this document we explain important updates to our analytical procedures and some caveats relevant to sample packaging and handling, laser heating and temperature measurement, gas gettering and monitoring, and data collection and reduction.

1. Sample packaging and handling

Each apatite grain, after being picked and photographed, was packaged in a niobium (Nb) tube with both ends closed – a standard approach for single-grain apatite (U-Th)/He dating. The tube was then wrapped in a Nb foil envelope (Fig. B1A). The Nb tubes we used for these experiments had an outside diameter of 0.4 mm and length of 0.7 mm. The foil envelopes were octagonal-to-circle shaped with a diameter of ~2 mm, a size chosen to fit into the indentation in a cylindrical quartz glass sample holder (Fig. B1B) and also to completely contain the measurement spot of the optical pyrometer (~1.1 mm). The holders fit into a sample rack fitted with a linear

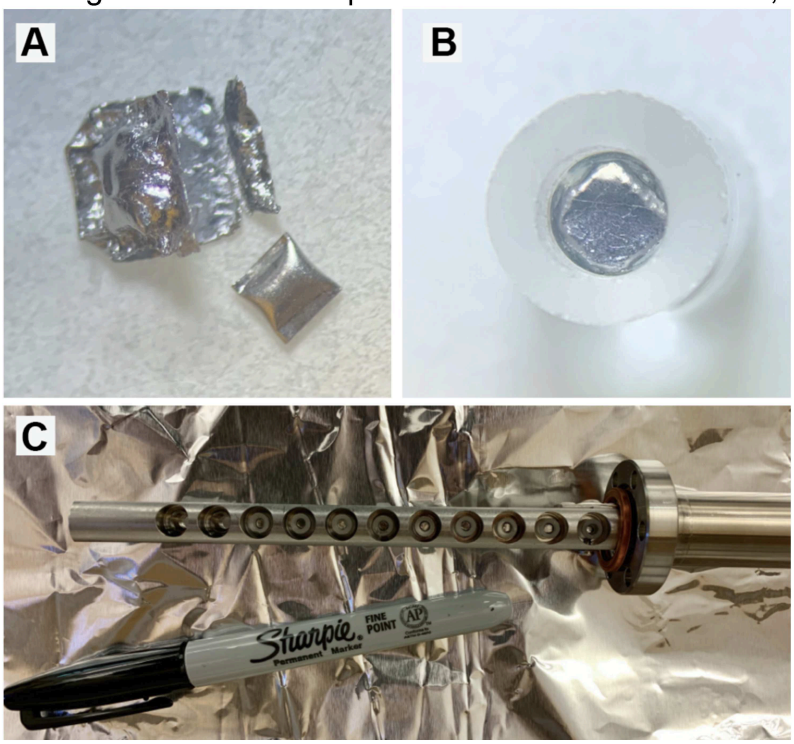

Figure. B1: Sample packaging.

actuator that allows up to 12 samples to be positioned under the laser beam (Fig. B1C). Both the Nb tubes and foil envelopes were cleaned with 7% HNO_3 and degassed for 3 hours in a vacuum furnace at 600 °C before packaging. The overall goal of our packaging strategy is to keep the sample packet as small as possible in order to allow efficient and responsive laser heating (see following section) while still providing enough packet surface area for accurate temperature measurement.

2. Laser heating and temperature measurement

The TAM samples were heated with a 30 watt 808 nm fiber-coupled diode laser, and their temperatures were monitored using a BASF Exactus optical pyrometer positioned coaxially with the laser beam path as part of a custom beam delivery system. The pyrometer was recalibrated every 8-12 sample runs against a K-type thermocouple embedded in a “dummy” sample packet in one of sample-rack positions. Temperature regulation was achieved by modulating the laser power under closed-loop PID control using a custom Labview program. For the TAM experiments we performed CRH analysis using a heating rate of 30 °C/min. This rate was chosen to balance the responsiveness of the temperature control system, the speed of ^{4}He flow and pressure equilibration within the extraction line, the efficiency of active gas cleanup, and the time needed for the ^{4}He signal to be integrated and recorded with sufficient precision.

3. Gas gettering and monitoring

CRH analysis involves continuous sample heating and measurement of released helium gas under static conditions with the sample chamber open to the mass spectrometer.

The presence of other active gas components released from both the sample and the extraction system will impact CRH analysis and therefore requires careful attention to gettering and monitoring of these active gas contaminants. We have found that hydrogen and nitrogen in particular can alter the effective ^{4}He sensitivity via pressure scattering or possibly other source effects. For the TAM experiments we used two SAES GP-50 getters operated at 20 and 200 °C in the extraction line for active gas cleanup, as described by Idleman et al. (2018). Fortunately, laser heating is particularly advantageous for CRH analysis, as the much smaller heated area relative to that required for furnace-heating experiments helps to minimize the evolution of these active gases. With our current laser heating setup, hydrogen and nitrogen co-evolved with ^{4}He have the greatest impact on the effective ^{4}He sensitivity at temperatures where the sample is almost completely degassed (i.e., > 850 °C) and can result in slight (~1-5%) underestimations of the final ^{4}He abundance. This problem can be addressed effectively by delaying the final measurement of the total ^{4}He beam intensity for ~3 minutes after the termination of laser heating, allowing the partial pressures of the active gas contaminants to fall to levels at which their suppression of the ^{4}He signal is trivial.

4. Data collection and reduction

The ^{4}He measurements were performed using a Pfeiffer Prisma Plus quadrupole mass spectrometer fitted with a channel electron multiplier. The CRH measurements were made in the static mode with the quadrupole fully open to the sample chamber.

The following sections highlight three key steps in our strategy for data collection and reduction:

Before heating. We allowed at least two minutes of measurement of the dynamic background in order to quantify the residual ^{4}He signal present before the extraction line was valved off from its pumps. Once the pump valve was closed, we performed another two to three minutes of measurement of what we found to be a linearly rising time-dependent static ^{4}He blank, allowing us to calculate the blank contribution over the course of the CRH experiment by extrapolation of these early measurements. In practice, we have found that the magnitude of this time-dependent static blank far exceeds the blank component contributed by sample heating, which in most experiments is trivial.

During heating. Temperature recording was initiated shortly before the start of laser heating. For the remainder of the experiment sample temperature and the ^{4}He beam intensity were recorded at fixed intervals of 10 s and 10.2 s, respectively. During the first 10-20 seconds of the experiment the samples were heated rapidly to ~160-170 °C under manual control to bring them within the measurement range of the pyrometer. After the sample temperature had stabilized for a few seconds control was passed to the Labview software, which then proceeded with the programmed heating schedule under closed-loop control. Heating and ^{4}He measurement continued until the sample was completely outgassed, as indicated by either a stable ^{4}He beam intensity for at

least one minutes or, more often, a slightly decreasing signal owing to the buildup of active gases.

After heating. After a sample was completely outgassed, we stopped temperature recording and allow the system to cool for three minutes, during which we commonly observed a 1-5% increase in the ^{4}He beam current until the beam current finally stabilized. This increase typically coincided with an orders-of-magnitude drop in the m/e 2 and 28 beam intensities as the sources of coevolved H_2 and N_2 cooled and these gases were gettered. We used the final ^{4}He beam intensity achieved after this cleanup step for the age calculation. Once the ^{4}He beam had been measured we introduced a calibrated aliquot of ^{4}He as a standard addition to establish the ^{4}He sensitivity of the quadrupole.

After completion of a CRH experiment, temperature and ^{4}He abundance data were synchronized by linear interpolation using the time stamps recorded with each measurement. The accumulated ^{4}He blank (static blank) was calculated using the previously determined accumulation rate and the heating duration. We then subtracted the dynamic background and the time-dependent static blank from our measured ^{4}He beam currents before calculating cumulative ^{4}He loss as a function of temperature (f), and differentiation of the cumulative loss curve to obtain fractional loss (df/dT).